



UNIVERSITY OF LEEDS

This is a repository copy of *A geostatistical approach to analyzing gold distribution controlled by large-scale fault systems – An example from Côte d'Ivoire*.

White Rose Research Online URL for this paper:  
<http://eprints.whiterose.ac.uk/140954/>

Version: Accepted Version

---

**Article:**

Murray, S, Torvela, T [orcid.org/0000-0003-1539-8755](https://orcid.org/0000-0003-1539-8755) and Bills, H (2019) A geostatistical approach to analyzing gold distribution controlled by large-scale fault systems – An example from Côte d'Ivoire. *Journal of African Earth Sciences*, 151. pp. 351-370. ISSN 1464-343X

<https://doi.org/10.1016/j.jafrearsci.2018.12.019>

---

© 2019 Elsevier Ltd. All rights reserved. Licensed under the Creative Commons Attribution-Non Commercial No Derivatives 4.0 International License (<https://creativecommons.org/licenses/by-nc-nd/4.0/>).

**Reuse**

This article is distributed under the terms of the Creative Commons Attribution-NonCommercial-NoDerivs (CC BY-NC-ND) licence. This licence only allows you to download this work and share it with others as long as you credit the authors, but you can't change the article in any way or use it commercially. More information and the full terms of the licence here: <https://creativecommons.org/licenses/>

**Takedown**

If you consider content in White Rose Research Online to be in breach of UK law, please notify us by emailing [eprints@whiterose.ac.uk](mailto:eprints@whiterose.ac.uk) including the URL of the record and the reason for the withdrawal request.



[eprints@whiterose.ac.uk](mailto:eprints@whiterose.ac.uk)  
<https://eprints.whiterose.ac.uk/>

1 **A geostatistical approach to analyzing gold distribution controlled by large-scale fault systems**  
2 **– an example from Côte d'Ivoire**

3 Sarah Murray<sup>a</sup>, Taija Torvela<sup>a,\*</sup>, Howard Bills<sup>b</sup>

4 <sup>a</sup>Ores and Mineralization Group, University of Leeds, School of Earth and Environment,  
5 Leeds, LS2 9JT, United Kingdom

6 <sup>b</sup>ToroGold Limited, Piccadilly, St. James's, London W1J 9EJ, United Kingdom

7 \*Corresponding author. E-mail address: t.m.torvela@leeds.ac.uk (T. Torvela).

8 *Abstract*

9 Geostatistical approaches can help to understand the general characteristics of an area, to  
10 suggest feasible geological models, and to quantify overall patterns in the occurrence of  
11 economic mineralisation. We use such an approach to demonstrate the relationships  
12 between large-scale faults of various ages and kinematics, lithologies, and gold  
13 mineralisation to facilitate understanding of crustal-scale structural controls of gold deposits.  
14 Our example comes from Côte d'Ivoire, which is known to have undergone at least three  
15 major phases of deformation, two of which produced transpressional faults resulting from  
16 ESE-WNW and, later, NE/ENE-SW/WSW, compression. Using aeromagnetic and surface  
17 geological data, we interpret these faults and suggest a multiphase Riedel model for the  
18 region, taking fault reactivation into consideration. With the help of this simplified model, the  
19 spatial relationships between the faults, lithology, and 909 known gold occurrences,  
20 including 554 artisanal mining sites, are analysed within a GIS. Using geostatistical methods,  
21 gold mineralisation was found to probably be a two-stage process, with the later D2 stage  
22 potentially being the peak mineralization event. Gold occurrences are most abundant within  
23 c. 3 km of both newly formed and reactivated NE-SW faults, most importantly P1 and Y2  
24 faults, in areas of low-intermediate fault density, and close to lithological contacts within the  
25 greenstone sequences.

26 Keywords: gold, geostatistics, GIS, structural geology, Riedel fault model, fault reactivation,  
27 Côte d'Ivoire

28

## 29 *1. Introduction*

30 Understanding the general geological characteristics of any area can be a major asset in  
31 both scientific and applied investigations. For example, exploration methods often include  
32 the identification of geological features similar to those which have already proven  
33 prospective. Geostatistical approaches, while often simplified by necessity, are an important  
34 tool that may provide additional insights into the characteristics of an area, and help in  
35 suggesting feasible geological models. Models that quantify relationships between mineral  
36 deposits and geological features may prove useful in identifying effective exploration  
37 strategies and new exploration targets at a regional scale. In this paper, we use GIS analysis  
38 of a crustal-scale fault interpretation to investigate and quantify relationships between crustal  
39 structures and gold mineralisation in Côte d'Ivoire. The interpretation is gained from  
40 geophysical data and geological maps and underpinned by published field data and  
41 estimates on the palaeostress field orientations. The presented spatial statistics and their  
42 analysis show that there is a clear dependence between gold mineralisation and the  
43 orientation of the structures with respect to the palaeostress fields. We suggest a two-phase  
44 Riedel model to explain the general structural trends in this part of the West Africa craton  
45 and how these structural trends may relate to gold mineralization.

## 46 *2. Geological setting*

47 The West African Craton contains economic gold deposits in multiple countries including  
48 Côte d'Ivoire, Ghana, Burkina Faso, and Mali. In Côte d'Ivoire, economic deposits are found  
49 primarily within the Palaeoproterozoic Birimian greenstone belts. This greenstone covers  
50 much of the W African craton and consists of metamorphosed volcanic rocks, volcano-  
51 sediments and turbidites (Fig. 1; e.g. Eisenlohr, 1992; Milési et al., 1992; Vidal and Alric,

52 1994; Hirdes et al., 1996; John et al., 1999; Coulibaly et al., 2008; Berge, 2011; Metelka et  
53 al., 2011; Nyame, 2013).

54 The geology of Côte d'Ivoire can be split into two main sections (Fig. 1): the Kenema-Man  
55 terrane in the west, where the Palaeoproterozoic rocks have been thrust over the Archean  
56 gneisses (e.g. Milési et al., 1992; Marcoux and Milési, 1993; Camus et al., 2008), and the  
57 rest of the country where the basement consists of Palaeoproterozoic juvenile crust formed  
58 between c. 2.25-2.05 Ga and subsequently deformed (mostly during the Eburnean orogeny  
59 between c. 2.2-2.0 Ga; Table 1; e.g. Vidal and Alric, 1994). We focus on the  
60 Palaeoproterozoic rocks as these form most of the basement in Côte d'Ivoire and host a  
61 majority of the country's gold deposits (e.g. Coulibaly et a., 2008; Vidal et al., 2009; de la  
62 Mare, 2010). The Birimian, like many other greenstone terranes, is structurally complex, but  
63 overall shows many similarities with other Palaeoproterozoic and Archaean greenstone belts  
64 in which wide range of research exists and on which the widely accepted models for  
65 'orogenic gold' are based (e.g. Goldfarb et al., 2005). In these areas, gold is often late-  
66 orogenic, occurs within greenstones, and is closely associated, but not usually within, the  
67 large shear zones such that most gold deposits occur within secondary and tertiary  
68 structures; these are often locally extensional (even when the overall late-orogenic  
69 deformation may still be transpressional; e.g. Cox, 1999).

70 The early Palaeoproterozoic lithologies in Côte d'Ivoire and elsewhere in this part of W Africa  
71 consist of belts of Birimian greenstone squeezed between elongate granitoid complexes  
72 (e.g. Milési et al., 1991; Vidal et al., 2009). The greenstones are interpreted as  
73 volcanosedimentary sequences in origin and consists chiefly of turbidites, quartzites,  
74 carbonates, pelites, and banded iron formations interbedded with metamorphosed  
75 volcanoclastics, rhyolites, andesites, and basalts (Vidal and Alric, 1994; Vidal et al., 2009;  
76 Waller et al., 2015). Some authors suggest that deposition of all of these volcanosedimentary  
77 sequences was approximately contemporaneous (Nyame, 2013), but some age evidence  
78 contradict this and indicate two distinct volcanic belts forming at c. 2.2 Ga in the east and c.

79 2.1 Ga in the west (Hirdes et al., 1996). The NE-SW trending belts are separated by the  
80 Eburnean granitoids, consisting of a an older c. 2.2 Ma phase of Tonalite-Trondjemite-  
81 Granodiorite (TTG) plutons and a slightly younger c. 2.1 Ma phase of leucogranite intrusions  
82 (Vidal and Alric, 1994; Vidal et al., 2009). These units have been unconformably overlain by  
83 the Tarkwaian sediments in the east part of the country (Milési et al., 1991). This fluvio-  
84 deltaic quartz-pebble conglomerate deposited ~2.1 Ga, and is thought to consist of eroded  
85 Birimian material, possibly deposited during a short extensional phase or within an intra-  
86 orogenic basin (Milési et al., 1991; John et al., 1999; Camus et al., 2008; Baratoux et al.,  
87 2011; Augustin et al., 2017).

88 The main metamorphism and deformation of the Palaeoproterozoic West African crust  
89 occurred as a result of the Eburnean Orogeny with a c. NW-SE oriented  
90 compression/transpression (D1; Table 1; e.g. Marshak, 1999; Vidal et al., 2009; Criddle et  
91 al., 2011). In the Birimian units, the metamorphic grade did not in most areas exceed  
92 greenschist facies (e.g. Eisenlohr and Hirdes, 1992), although some areas in Côte d'Ivoire  
93 and elsewhere in W African Craton have experienced up to granulite facies conditions during  
94 the Eburnean (e.g. Pitra et al., 2010; Block et al., 2015). A literature review of the Eburnean  
95 orogeny and the earlier events is beyond the scope of this paper, but one of the main  
96 debate points relates to whether the initial, 'dome-and-keel' style structure of Côte d'Ivoire  
97 formed as a result of the theoretical 'Archaean-style' crustal growth by diapiric magmatism  
98 (e.g. Vidal et al., 2009) or as a more 'modern-style' tectonics of a hot orogen with syn- or  
99 post-orogenic collapse (e.g. Marshak, 1999). For the purposes of this study, the importance  
100 of the early D0 events lies solely in their geometric configuration; by the time interval of  
101 interest to this paper (2.2-1.8 Ma, i.e. D1-D2), the overall crustal shortening occurred in a  
102 thrust-style tectonics as the related geometries formed in their approximate present locations  
103 and the fault zones are seen to systematically affect and deform most of the intrusions and  
104 dome features. The detailed tectonic style of events up to 200 Ma earlier (i.e. diapiric vs.  
105 modern style tectonics) is not, therefore, discussed here..

106 Details of the Eburnean orogenic and post-orogenic evolution at c. 2.2-1.8 Ma are debated  
107 and multiple phases of deformation have been suggested (e.g. Milési et al., 1992; Metelka  
108 et al., 2011; Traoré et al., 2016) although it seems likely that the Eburnean orogenic  
109 evolution was a continuum with progressively clockwise-rotating compression, similar to  
110 most transpressive orogens (Augustin et al., 2017). For example, Vidal et al. (2009)  
111 comment on two phases during the Eburnean Orogeny, whereas e.g. Milési et al. (1992) and  
112 Camus et al. (2008) discuss three phases. Further, it is somewhat unclear when exactly  
113 during the Eburnean phase at c. 2.2-2.0 Ga the overall 'thickening phase' dominated by  
114 thrust tectonics gave way to strike-slip dominated tectonics, but it occurred after the ~2.1 Ga  
115 solidification of the early Eburnean leucogranites (e.g. Jessell et al., 2012). Either way, it is  
116 generally agreed that the direction of the regional maximum compressive stress during the  
117 main Eburnean phase was approximately NW-SE. The orientation of the stress field that was  
118 superimposed on the Eburnean deformation soon after the this phase (c. 2.0-1.8 Ga) is more  
119 controversial but was approximately NE-SW to E-W (e.g. Eisenlohr and Hirdes, 1992; Vidal  
120 and Alric, 1994; Baratoux et al., 2015; Traoré et al., 2016; Augustin et al., 2017). Some  
121 works suggest a final, non-mineralizing, c. N-S oriented compression stage of an unknown  
122 age, resulting in some E-W striking reverse faults and crenulation cleavages superimposed  
123 on previous fabrics (e.g. Baratoux et al., 2015). For the purposes of this paper, the published  
124 data allow us to simplify this overall tectonic evolution and the related gold mineralization  
125 stages and use D1 for the main Eburnean phase with approximately NW-SE compression,  
126 and D2 for the 'post-Eburnean', c. E-W directed compressional event (Table 1). These  
127 published palaeostress field orientations underpin our fault evolution models.

128 Given the multiple phases of deformation, structural reactivation can be considered highly  
129 likely in the area given that the amount of stress required to create new faults is much higher  
130 than what is necessary to reactivate existing structures (Sibson, 1985). Although many  
131 parameters such as pore fluid pressure, fault roughness, lithology and mechanical  
132 stratigraphy, and inherited/pre-existing weakness zones are important in fault reactivation,

133 the fault orientation relative to the stress field is considered to be the most influential factor:  
134 the angle between the maximum principal stress  $\sigma_1$  and the fault orientation must be  
135 contained within a window so as to have some resolved shear stress (Fig. 2; Fossen, 2010).  
136 Our interpretation and analysis makes an attempt to assess the fault reactivation likelihood,  
137 and the importance of the reactivation to gold mineralization, based on these principles.

### 138 *2.1 Style of gold mineralisation*

139 Globally, 'orogenic' gold, or 'lode' gold, mineralisation is often associated with, but not  
140 necessarily hosted by, major crustal structures (e.g. Cox, 1999). Higher grade mineralisation  
141 is often, although not always, found in quartz veins within or near second-order low-  
142 displacement faults related to the major structures: these low order networks, such as fault  
143 splays where fluids can become trapped, are connected at one end to higher order  
144 structures but can also be semi-independent such as fractures and faults at fault jogs and  
145 relay ramps (Fig. 3; e.g. Cox, 1999; Groves et al., 2000; Hagemann and Cassidy, 2000;  
146 Goldfarb et al., 2005). However, at a crustal scale, the major structures are interpreted to act  
147 as a first-order control of lode gold mineralization as they form the backbone for fluid flow  
148 (e.g. Sibson et al., 1988; Cox, 1999). Although little information is available on the details of  
149 most gold-controlling structures within Côte d'Ivoire, many deposits in the country and within  
150 the equivalent geological terranes in neighbouring Ghana and Burkina Faso are described  
151 as closely associated with large NE- SW trending faults and shear zones at a regional scale  
152 (Hagemann and Cassidy, 2000; Béziat et al., 2008; Johnson et al., 2013; Ballo et al., 2016).

153 Most published works from the Birimian in West Africa are from the neighbouring countries  
154 rather than Côte d'Ivoire. These show that there are various styles of Eburnean-aged gold  
155 mineralization within the Birimian (e.g. Markwitz et al., 2016). A detailed review is beyond the  
156 scope of this paper: what is important here is that most of the gold mineralization is 'orogenic  
157 gold', i.e. structurally controlled and at least spatially associated with large shear/fault  
158 zones, while intrusion-related and skarn deposits do occur but are rarer (e.g. Camus et al.,  
159 2008; McFarlane et al., 2011; Johnson et al., 2013; Markwitz et al., 2016). Orogenic gold

160 commonly occurs in bedding- or lithological contact-parallel shears, in stockwork vein  
161 systems, and in quartz veins in both brittle and ductile shears, often within splays of the  
162 nearest regional shear zone (e.g. Berge, 2011; Baratoux et al., 2015; Ballo et al., 2016;  
163 Markwitz et al., 2016). The quartz-dominated vein systems commonly occur with small  
164 quantities of sulphides and carbonates (e.g. Béziat et al., 2008; Camus et al., 2008; Johnson  
165 et al., 2013). The timing of the mineralization in Côte d'Ivoire is somewhat unclear but it is  
166 generally agreed that the onset of gold mineralisation occurred at approximately 2.1-2.0 Ga,  
167 i.e. relatively late in the Eburnean tectonic evolution and similarly to the suggested peak Au  
168 mineralization within the W African Craton in general (e.g. Milési et al., 1991, 1992; Pigois et  
169 al., 2003; Béziat et al., 2008; Camus et al., 2008; Markwitz et al., 2016; Augustin et al.,  
170 2017). This is somewhat later than what is suggested for the neighbouring countries, where  
171 the first Au-mineralizing event is interpreted at 2.19-2.15 Ga (e.g. Allibone et al., 2002; Parra-  
172 Avila et al., 2015). It is also clear that the mineralization continued for some time after the  
173 main Eburnean phase, although the exact ages, extent and conditions of this late  
174 mineralization are debated: for example, Camus et al. (2008) propose three phases of  
175 hypogenic gold mineralisation in Côte d'Ivoire, each with generally lower grades than the  
176 previous: Au1 (2.17-2.12 Ga), Au2 (2.1-2.097 Ga), and Au3 (age unknown). In contrast,  
177 others postulate that it is the late, post-Eburnean mineralization event that was the most  
178 significant one (e.g. Milési et al., 1992). Still others suggest, based on studies in southern  
179 Mali, that there is evidence of long-lived gold mineralization and that all events were  
180 important, but locality-dependent so that certain deposits show significant gold mineralization  
181 related to structures formed in the late-Eburnean stress field, while in others the structures  
182 formed by the post-Eburnean E-W shortening were more important (Traoré et al., 2016).

### 183 *3. Data and uncertainties*

184 Aeromagnetic data flown by Kenting Exploration Services Limited 1974-1976 formed the  
185 majority of the data used (Table 2). The data covers most of Côte d'Ivoire and consists of the  
186 total magnetic intensity (TMI), analytical signal (AS), and vertical derivative (VD; Fig. 4A).

187 The data were collected by a fixed-wing aircraft flown along N-S flight lines at 150 m altitude  
188 with 500 m line spacing. In addition to the geophysical data, geological maps were available  
189 at a regional 1:1 000 000 scale (Bagarre and Tagini, 1965) and a local scale varying  
190 between 1:200 000 and 1:500 000 (Delor and Yao, 1998; Fig. 4B). The dataset was  
191 complimented with georeferenced locations of 910 known gold occurrences across the  
192 country (Fig. 5). The data were interpreted and analysed in ArcMap, as described in the  
193 following chapters.

194 Uncertainty inherent within the geophysical data include extrapolation between the flight  
195 lines, which can result in creation of geometric artefacts. This was taken into account when  
196 interpreting the geophysical data, so that care was taken with any features in both N-S and  
197 E-W directions. In addition, many of especially the c. WNW-ESE trending features are  
198 magnetic highs and likely to be dykes of unknown age (Jessell et al., 2015), although in  
199 some cases these dykes may utilize pre-existing faults. The fault interpretation itself carries  
200 an inherent uncertainty in terms of the detailed location and strike of the fault: the resulting  
201 fault strikes are by necessity approximations in detail, but are relatively robust at scales  
202 larger than a few kilometres. The general fault trends should, therefore, be relatively easy to  
203 establish.

204 Interpretation of the fault kinematic history is challenging even in the field and even more so  
205 using remote sensing. Remote interpretation is even more reliant on good-quality, high-  
206 resolution geophysical and geological data as, where field data are unpublished, large-scale  
207 kinematic markers such as deflected fabrics are used in kinematic interpretation. Despite  
208 their age, the geophysical data quality and resolution is mostly reasonable for the purposes  
209 of this study, but the geological maps are likely to be in need of revision and contain  
210 significant uncertainty. However, the dip of the deflected fabrics cannot in many cases be  
211 deduced from geophysical data, which may lead to misinterpretation of the shear sense.  
212 Fault reactivation may cause further complications if the sense of shear differs significantly  
213 from the original. At the scale of the structures addressed in this paper, the features and

214 geometries seen in the geophysical and published geological data are nevertheless  
215 reasonably consistent so that first-order estimation of the main fault kinematics and other  
216 major geological features such as the main lithological boundaries can be made. However,  
217 the resulting kinematic interpretations are inevitably generalizations and only one possible  
218 scenario: uncertainty exists due to the lack of more varied and detailed data, especially for  
219 the interpretation of the fault reactivations (see next chapter). The interpretation of any  
220 individual fault zone kinematics should ideally, therefore, be tested in the field. The statistical  
221 approach of this paper should aid in smoothing out any possible individual  
222 misinterpretations, revealing the main trends in the mineralization with respect to the fault  
223 type: as will be seen, the interpreted fault kinematics map relatively well into the published  
224 palaeostress directions and are coherent with respect to fault orientation, implying that the  
225 interpretations are reasonably robust at the scale of the study.

226 The Au occurrence distribution map also contains some uncertainty and bias. The  
227 information is unevenly distributed across the country; and only in a few cases there is any  
228 detailed information about the size or grade of deposits or the style of mineralization. The  
229 gold occurrence map, therefore, contains all known gold locations, regardless of size or  
230 grade. The map may also include some gold occurrences that are not controlled by faults.  
231 However, the distribution bias may well reflect the distribution of gold occurrences, in effect  
232 constituting a first-order filter of the data to exclude areas with little gold potential.  
233 Furthermore, as the aim of this paper is to investigate general trends in mineralization with  
234 respect to the structures, the grade and the size of any individual occurrence is considered  
235 to be of secondary importance. Finally, the published literature indicates that the vast  
236 majority of gold deposits are structurally controlled and, as will be seen in the following  
237 chapters, we have also included some quantitative assessment on the likelihood of the  
238 individual occurrences being fault-controlled vs. not fault-controlled. More detailed  
239 information such as grade or style of mineralization/deposit type on each deposit would,  
240 naturally, allow a more in-depth analysis of fault-gold relationships, and the lack of these

241 data restricts our study to a fairly general spatial assessment of these relationships. The  
242 interpretations and spatial statistics presented in this paper can nevertheless be used to  
243 suggest a geologically realistic model for the overall gold-fault relationships in Côte d'Ivoire.

#### 244 *4. Fault interpretation, fault models, and fault statistics*

245 Initial fault interpretation involved the identification of linear structures within the AS dataset  
246 with the help of the geological maps (Figs.5, 6). The TMI and VD were used to produce a  
247 more detailed interpretation where multiple faults and splays are located. The anisotropy of  
248 the TMI and VD were accounted for by correlating patterns within the AS.

249 The fault kinematic interpretations were underpinned by three basic relationships: km-scale  
250 deflection of fabrics; sigmoidal patterns within the fault zones; and fault orientations. The  
251 deflection of fabrics (geophysical or from geological maps/published literature) and sigmoidal  
252 or other asymmetric geophysical fabrics were used as the primary kinematic indicators.  
253 These were supported by interpretation based on fault orientation where geological and  
254 geophysical information alone was insufficient for kinematic interpretation: in the fault  
255 orientation-based approach, the published palaeostress field orientations were assessed in  
256 relation to the fault orientation, allowing a rough interpretation of fault kinematics. In other  
257 words, this meant that in case there were no other clear kinematic markers present, the  
258 published stress orientations were used to suggest the strike-slip fault kinematic component,  
259 based on the relationship between the maximum principal stress and the fault strike.  
260 Naturally, the interpretational uncertainty for the fault kinematics assessed in this way is  
261 larger than for those faults that were interpreted using geological or geophysical markers,  
262 but it is a geologically feasible approach to suggest one realistic scenario that takes into  
263 account the available data.

264 In terms of the observed sigmoidal patterns, these may result from e.g. minor local, rotated  
265 faults, splays, or strike-slip duplexes (e.g. Woodcock and Fischer, 1986; Viola et al., 2004).  
266 Therefore, their asymmetries can be used as kinematic indicators for the faults with which

267 they are associated. As the sigmoidal patterns are restricted to the interpreted faults and are  
268 not normally observed outside them, they can be separate from any observed deflected  
269 foliations/fabrics which occur at larger scales (and which in some cases may result in  
270 kinematically opposite interpretation, i.e. potential fault reactivation; e.g. Fig. 6D). Both the  
271 fault and sigmoidal patterns are in general at a scale larger than the survey flight line  
272 spacing, and along orientations (mostly SW-NE and NW-SE) that make it unlikely for them to  
273 be artefacts resulting from signal extrapolation between flight lines. In some cases, the fault  
274 orientation or surrounding geological fabrics vs. sigmoidal geometries gave contradicting  
275 indications of kinematics; in most cases these were interpreted to reflect D1 fault reactivation  
276 during D2, with the occurrence of both sinistral and dextral phases of deformation. This  
277 interpretation was only considered feasible when the fault orientation and the interpreted  
278 reactivation kinematics were consistent with the D2 palaeostress field orientation. It should  
279 be noted, nevertheless, that of all the fault kinematic analyses, the interpretation of D2  
280 reactivation of D1 structures probably carries the highest uncertainty.

281 Typically for fault zones, the overall pattern is of a series of linear fault zones cross cutting  
282 each other in a variety of directions. However, when observed at large scale on one hand,  
283 and plotted into rose diagrams on the other hand, the apparent fault strikes and the  
284 interpreted kinematics at the scale of the country reveal an overall pattern mostly  
285 corresponding to the Riedel fault model (Fig. 7). The main palaeostress field orientations,  
286 according to published literature, are approximately NW-SE/NNW-SSE for D1 maximum  
287 principal stress ( $\sigma_1^A$ ), and approximately E-W for D2 maximum principal stress ( $\sigma_1^B$ ). We use  
288 the observations of the Riedel geometries and the background literature on palaeostresses  
289 to construct a multi-phase Riedel model to classify the interpreted faults for further analysis.  
290 The classification is a generalization accounting for the slight variations in strike, probably  
291 arising from changes in the mechanical strength of different lithologies and/or multiple  
292 faulting episodes, although we also quantitatively assess and discuss the strike variations  
293 below. It is recognised that at least some of the large N-S striking faults probably initiated

294 during D0 (Table 3), but for simplicity they are assigned to the D1 phase as they are seen to  
295 cut D0 lithologies and, therefore, were active during D1. Any faults that did not fit the primary  
296 i.e. D1 phase Riedel model ( $M^A$  in Fig. 7B) in terms of their orientation and kinematics, were  
297 observed to fit with, and therefore assigned to, the later palaeostress field of D2 phase  
298 (Riedel model  $M^B$ ).  $M^B$  also takes into consideration the likelihood of reactivation of D1  
299 structures during D2 where they are in an optimal angle with  $\sigma_1^B$  (Table 3; Sibson, 1985).  
300 This was especially considered for faults that showed opposing kinematic indicators as  
301 described above. Structures with uncertain kinematics were assigned to the best-fitting  
302 Riedel structure.

303 It is often difficult to assess the dip-slip component of the displacement from remote sensing  
304 data. Our interpretation did not initially assign a dip-slip component to most of the faults.  
305 Most of the large-scale faults in the Birimian are steep, and both field and modelling studies  
306 imply that they are mostly strike-slip at least during the late phase of D1 as they affect the by  
307 then solidified Eburnean leucogranitic bodies (Table 1; e.g. Jessell et al., 2012; Baratoux et  
308 al., 2015;). It is, nevertheless, possible or even likely that many of the faults have  
309 experienced dip-slip or oblique movements at some point in their kinematic history (e.g.  
310 Baratoux et al., 2011). Indeed, e.g. Eisenlohr and Hirdes (1992) interpret c. NE-SW striking  
311 regional thrusts and reverse faults that are likely to originate early in D1 while  
312 compressional/transpressional deformation and crustal thickening was still predominant over  
313 strike-slip kinematics. Our models do suggest that some of the interpreted faults should be  
314 thrusts in approximately the same NE-SW orientation (the X1 faults in our model  $M^A$ ). Our  
315 model  $M^B$  also suggests another dominantly reverse fault group striking c. NW-SE (X2; Fig.  
316 7B) although these faults are fairly rare with only 23 interpreted faults assigned to this group  
317 (Table 3).

318 Although the overall Riedel geometries of the faults are readily observable in e.g. Fig 7A,  
319 deviations in the models from the idealized model  $M^I$  are evident as the fault strikes are  
320 rarely straight. This is illustrated in Fig. 8 where the faults strikes are separated depending

321 on the lithology they affect (Fig. 8; note that this figure is merely meant to illustrate the strike  
322 variability; the various strikes are not weighed according to the total fault length in each  
323 strike direction). The variation is usually less than 45°. However, there are some anomalous  
324 results which reflect a significant local change in the overall fault strike as it intercepts  
325 another lithology, presumably due to the rheological contrast between these lithologies. The  
326 notable anomalies were investigated and most were found to occur where a small section of  
327 the fault length or a curved fault tip passes through the Precambrian gneisses and granites,  
328 the dolerites, Tarkwaian sediments, or amphibolites. These lithologies are a small minority of  
329 all lithologies in terms of their area of exposure, and, as will be discussed below, contain  
330 very few gold occurrences: therefore, we consider that the anomalies listed above are  
331 inconsequential in the context of this paper. However, there are other anomalies that may be  
332 of significance. For example, the apparent strike variations in R1 structures within the main  
333 lithologies are fairly significant in this figure (although their general strikes are more obvious  
334 from Fig. 7A): the strikes range from c. NNW-SSE orientations within the Eburnean  
335 granitoids to NNE-SSW strikes within the turbiditic and volcano-sediments. The strike  
336 variations possibly result from control of pre-existing basement precursors as especially the  
337 N-S structures may have initiated during D0, but the mean strike calculation method in  
338 ArcGIS may have played a role as well. The mean strike is calculated using the linear  
339 directional mean tool within ArcGIS: this tool produces vectors representing the mean length  
340 and strike of each structure type positioned in the spatial centre of the input data (Table 3;  
341 Esri, 2016b). The method analyses the attributes of the straight line between the end points,  
342 not accounting for any fault bends. Therefore, if the fault tips have a slightly different strike  
343 than the main fault body, the resulting calculated mean strike may differ significantly from the  
344 strike of the main body of the fault. This is especially true for R1 which shows multiple bends  
345 at fault tips (Fig. 7A). The fault bends are reflected in the vector attribute circular variance  
346 (CV; Table 3) which provides a numerical representation of how well the vector fits the data  
347 in a similar fashion to standard deviation (Esri, 2016b). Therefore, CV is a good estimation of  
348 fault straightness. The median CV is 0.012, which indicates a reasonable overall fit to their

349 assigned Riedel structure and relatively straight faults. R1 faults are seen to have an  
350 anomalously large CV of 0.567. Many R1 structures curve into horsetail splays at each fault  
351 tip (Fig. 7A) making the direct route between endpoints oblique to the strike of the main  
352 length of the fault. This results in a high CV, and also skews the mean strike of the R1  
353 structures: the main length of the majority of R1 structures strike c. N-S despite the  
354 calculated mean strike of c. 21°. This was corrected in M<sup>A</sup> by incorporating in to the model  
355 the dominant N-S strike (rather than the 21°) which was gained from eliminating the fault tips  
356 from the R1 interpretation to produce a more accurate representation of this fault class (Fig.  
357 7B). R1 has also the longest average length at 37.3km, against the average length of all  
358 faults of c. 23km, although Y1 faults are also very long at 36km. The average length of D1  
359 faults is c. 50% higher than the length of the D2 faults (27km vs. 18km, respectively).

360 Some key plots of various attributes are shown in Fig. 9, from which some potentially  
361 important observations can be made. Based on the published literature, and adopted in the  
362 Riedel models in Fig. 7B, the plots assume maximum principal palaeostresses of  $\sigma_1^A$  (D1) at  
363 155°-335° i.e. NW-SE, and  $\sigma_1^B$  (D2) at 85°-265° i.e. ENE-WSW, which approximately match  
364 the angle bisector between the R and R' faults in both models. Due to the generally higher  
365 CV of D1 structures, there is more uncertainty to the palaeostress field orientation for D1,  
366 while the low mean (and average) CV for D2 structures indicate that the estimated  $\sigma_1^B$   
367 should be a fairly good fit for the interpreted D2 faults. Either way, changing the palaeostress  
368 field orientations by c. ±5° does not significantly influence the general plot patterns and the  
369 observations made below.

370 The fault length broadly correlates inversely with fault count (Figs. 9A, B). This can be  
371 expected if it is assumed that, during fault evolution, a large number of smaller faults  
372 generally tend to link to form fewer, longer faults (e.g. Peacock and Sanderson, 1991). There  
373 are notable deviations: for D1 faults, there seem to be very few R'1 structures considering  
374 their length. P1 is deviating slightly from the trend, as it has a relatively large mean length of  
375 c. 27km but also a high total count of 150. For the D2 faults, Y2 with a modest average

376 length of 20km is clearly anomalous with a high total count of 138. R'2 is also clearly  
377 anomalous: similarly to R'1, this fault type has a very low count considering its relatively  
378 short length. For the other D2 faults, the fault count drops more rapidly with increasing fault  
379 length than D1 faults; the cause of this is unknown. The D1 fault lengths do not correlate  
380 with their reactivation percentage; the longer faults do not seem to be more susceptible for  
381 reactivation (not plotted: see Table 3).

382 There seems to be variable correlation between the angle between  $\sigma$  vs. fault strike and the  
383 total count or reactivation tendency of faults. For D1 (Figs. 9C), faults R'1 and R1 have an  
384 angle with respect to  $\sigma_1$  closest to the ideal  $30^\circ$ , but this does not seem to result in a higher  
385 total fault count; P1 which has the highest count of the D1 faults has an angle of c.  $63^\circ$ . It  
386 should be noted that, if the kinematic interpretation is mostly correct for P1 faults, they  
387 cannot be easily assigned to D2 as the kinematics do not match with the D2 stresses. X1  
388 which according to the model is a reverse/thrust fault has a high angle of  $75^\circ$  (faults in this  
389 orientation have also been interpreted as thrust by e.g. Eisenlohr and Hirdes, 1992). R1,  
390 which is the longest fault population, shows a slightly lower total count than Y1 despite their  
391 very similar angles. D2 faults (Fig. 9D) show that Y2 and R2 have a high total count; both  
392 formed at an angle quite close to the ideal  $30^\circ$  with respect to  $\sigma_1^B$ . On the other hand, R'2  
393 has a close-to-ideal angle as well but a very low count. P2 has a fairly low count at an angle  
394 of c.  $44^\circ$ , with the reverse/thrust X2 faults again showing a high angle of c.  $75^\circ$ . Of the D1  
395 faults reactivated during D2 (Fig. 9E), there is a good correlation between the fault angle and  
396 reactivation tendency, although P1 is again slightly anomalous with 86% reactivation despite  
397 its somewhat high angle of  $48^\circ$  with respect to  $\sigma_1^B$ . The CV or the average length of the D1  
398 faults do not appear to influence reactivation of the structures during D2 (plot not shown).

399

400 5. *Gold statistical data analysis*

401 5.1 *Lithology vs. gold*

402 The effect of lithology on mineralisation was investigated through the number of gold  
403 occurrences per km<sup>2</sup> (Au/km<sup>2</sup>) of each lithology within a buffer zones of various radii (Fig.  
404 10). The small area of Tarkwaian conglomerate and Precambrian gneiss occurring within the  
405 15km radius of faults contained very few gold occurrences (<2% of the total). Given the  
406 small area of these lithologies, the results did not represent the dataset as a whole and so  
407 were excluded to prevent skewing of the data. Of the major lithologies within 15 km of a fault  
408 (Fig. 10A), the volcano-sediments were seen to include the most occurrences (0.014Au/km<sup>2</sup>)  
409 whilst the Eburnean granite hosts the least (0.0015Au/km<sup>2</sup>). However, closer to the major  
410 faults, there is more equal distribution between the three main rock units, although the  
411 volcanoclastics are still the dominant lithology (Fig. 10B, C).

412 5.2 *Fault density*

413 One of the potential controls on the gold mineralization is imposed by the fault density, which  
414 may correlate directly with fault connectivity. We used two statistical tools in ArcGIS to  
415 assess the relationship between fault density and gold occurrence: kernel density and line  
416 density. In an attempt to also analyse the impact of major structures (faults accommodating  
417 significant displacement) on mineralisation, the resulting fault density maps were also  
418 weighted by fault length, assuming that longer faults accommodate more displacement (e.g.  
419 Walsh and Watterson, 1988; Peacock and Sanderson, 1991; Cartwright et al., 1996).

420 Of the two, the line density method proved to be more reliable as the kernel density method  
421 produced some obvious artefacts (i.e. indicated high fault densities where no faults had been  
422 interpreted). The line density method creates a circular neighbourhood, set at 15 km,  
423 around each raster cell, then calculates the total line length enclosed within each  
424 neighbourhood and divides by its area. This method produces an initial density map  
425 reflecting the observed fault distribution fairly well with no obvious anomalies (Fig. 11A). The

426 pattern consistently follows major trends and splays with some peaks around particularly  
427 densely populated areas. The fault density map can then be compared to the gold  
428 occurrence map: of a total of 909 occurrences, 891 Au occurrences are found to show some  
429 correlation with this fault density map (Fig. 11B). 50% of these gold occurrences are located  
430 in areas of a fault density less than  $0.077\text{km/km}^2$  whereas 85% of the occurrences are within  
431 areas of fault density of  $0.155\text{ km/km}^2$  (Fig. 11B).

432 When the faults are weighted by their length to reflect their relative displacement (by  
433 multiplying the fault length contained within each neighbourhood by its own total length), the  
434 resulting density map is very similar to the non-weighted map but with areas of higher  
435 density focussed around longer faults (Fig. 12A). Most of these gold occurrences are,  
436 similarly to the non-weighted map, located in low-intermediate density areas with 50% of  
437 occurrences within c.  $2800\ \Sigma(\text{fault length} \times \text{total length})\text{km/km}^2$  and 85% within c.  $5200$   
438  $\Sigma(\text{fault length} \times \text{total length})\text{km/km}^2$  (Fig. 12B).

439 In each case, there is a peak in gold occurrences in areas of very low fault density, with  
440 another smoother peak around the median fault density. The non-weighted line density  
441 method (Fig. 11) calculates total fault length per area. Here, high density areas are the result  
442 of many faults within a small area and, therefore, give a probable indication of relative fault  
443 connectivity (high fault density suggesting potential for higher connectivity; e.g. Walsh et al.,  
444 1998). The observed relative paucity of gold occurrences within the high density areas  
445 suggests that gold is less likely to be deposited in the relatively high connectivity areas. This  
446 is unsurprising: it is a common feature in Precambrian greenstone terranes that gold is  
447 typically deposited in secondary or tertiary structures rather than the highly conductive main  
448 shear zone (e.g. Cox, 1999). The length-weighted method (Fig. 12) plots the highest fault  
449 densities along longer structures (major fault zones). Again, these high density areas show a  
450 relatively low quantity of gold occurrences, which suggests that gold is less likely to be  
451 deposited along major structures which are also likely to be high-connectivity structures.  
452 Where gold does occur in these high density areas, it is usually located around fault splays

453 at the edges of these areas, suggesting that the splays rather than the main faults have a  
454 connection with mineralisation.

### 455 *5.3 Distance between gold occurrences and faults*

456 Buffer zones of variable radii were created around gold occurrences and structures in order  
457 to investigate the basic spatial fault-gold relationships at the intersecting areas with the aim  
458 of excluding from the analysis those gold occurrences that do not show an obvious large-  
459 scale fault control. Gold occurring far away from regional faults may belong to the class of  
460 gold deposits interpreted to have magmatic origins (McFarlane et al., 2011; Johnson et al.,  
461 2013; Markwitz et al., 2016). Of a total of 909 occurrences, c. 769 occurrences are found  
462 within a 15km radius from any fault and were, therefore, interpreted to be potentially fault-  
463 controlled (Fig. 13A; Appendix A). The likelihood of the fault control is probably dependent  
464 on the distance to a fault: where the number of Au occurrences decrease approximately  
465 logarithmically with distance from the faults, we consider it more likely that the gold is  
466 controlled by the fault. This kind of rapid decrease away from the fault is best exemplified by  
467 fault Y2 (Fig. 13B) but also by faults Y1 and P1, whereas other faults such as R1 or P2 show  
468 little change in Au occurrence with distance (Fig. 13C; see also Appendix A). For all faults,  
469 50% of the 769 Au occurrences are present within c. 3.8 km of a fault, and 85% of the  
470 occurrences are present within c. 8.9 km of a fault (Fig. 13A; Table 3). As the distance of 3-4  
471 km seems, therefore, to be statistically significant, as is possibly the distance of c. 9 km,  
472 these distances were chosen for further analysis below.

#### 473 *5.3.1 Proximal structure vs. dominant structure*

474 The next consideration is to correlate the number of gold occurrences per fault type and the  
475 interpreted deformation phase. Two options are possible here for the gold occurrences that  
476 are likely to be fault-controlled : 1) the gold is controlled by the longest fault within a circular  
477 neighbourhood ('dominant structure'); or 2) the controlling structure is the fault that is closest  
478 to the gold occurrence ('proximal structure'). The rationale is that in the case of the 'dominant  
479 structure', the longest fault is likely to carry the most displacement and, therefore, the widest

480 damage zone and/or most sub-resolution lower-order structures into which the mineralizing  
481 fluids can migrate; whereas a 'proximal structure', while not necessarily being a major fault  
482 with significant displacement, is still likely to have a damage zone and lower-order structures  
483 that can host mineralization. For a number of gold occurrences, the dominant and the  
484 proximal structure is likely to be the same fault, but we will consider both structure types  
485 separately in order to distinguish any potential differences. Various buffer zones were tested,  
486 most importantly the 3 km buffer zone which hosts nearly 50% of all gold occurrences that  
487 are interpreted to be fault controlled (i.e. within 15 km of any fault), and the 9 km buffer zone  
488 which hosts >85% of all fault-controlled occurrences (Fig. 13A).

### 489 *5.3.2 Dominant structure*

490 The method used to analyse the dominant structure is similar to the line density  
491 methodology in that a circular radius neighbourhood is drawn around each raster cell. Each  
492 cell is then classified by the type of structure with the greatest length within the radius. As  
493 the timings of most gold formations are not known in detail with respect to the fault timings,  
494 this method was applied to all gold occurrences and all the faults. In an effort to potentially  
495 resolve gold mineralization timing as well as the basic fault strike-gold relationship, we also  
496 separated the faults based on their interpreted timing (D1 or D2), i.e. i) all newly formed D1  
497 faults; ii) all newly formed D2 faults; iii) all D1 faults interpreted to have been reactivated  
498 during D2; and iv) all faults existing during D2 regardless of whether they were active or not.  
499 Each analysis was normalized by dividing the number of gold occurrences within the  
500 neighbourhood by the length of each structure, in order to remove the bias caused by  
501 different lengths of each structure. Those faults of type R'1 and R'2 that showed any  
502 association with Au were too few in their total count (8 and 7, respectively: Appendix A) to be  
503 considered statistically reliable, and as they were seen to skew the results they were  
504 removed from this analysis. Fig. 14 summarizes the key results (i.e. the 3 km and 9 km  
505 buffer zone radii with the normalized analyses). The plots clearly show that the structures  
506 have very different potential for gold occurrence depending on their orientations.

507 Scenario i) i.e. all new D1 faults, is shown in (Fig. 14A). There are some differences between  
508 the 3 km and 9 km buffer zones, most notably the sharply increasing importance of X1  
509 within the 9km buffer zone,. P1 is the most important fault within both buffer zones. It is  
510 noted that Y1 and P1 have very similar strike.

511 Scenario ii) the newly formed D2 faults (Fig. 14B): here, X2 and Y2 are the dominant faults  
512 within both buffer zones, with X2 being more important than Y2 within the 3 km buffer zone,  
513 while the inverse is true for the 9 km zone. For scenario iii) i.e. all D1 faults reactivated  
514 during D2 (Fig. 15C), the reactivated P1 emerges again as a significant feature but Y1 is  
515 also important.

516 When scenario iv) i.e. all faults existing during D2 is considered, regardless of whether they  
517 were active or not, Y2 remains the most dominant structure followed closely by Y1 within the  
518 3 km buffer zone (Fig. 14D). Of the other faults within a 3 km radius, P1, R1, and R2 seem to  
519 be slightly more dominant than the rest, while P2 is the least dominant. This pattern changes  
520 when a 9 km radius is considered: X1 is the most dominant fault after Y1 and Y2, followed  
521 by P1 and R1. P2 and X2 remain insignificant.

### 522 5.3.3 Proximal structure

523 In this scenario, the closest fault to each gold occurrence, as opposed to the longest fault, is  
524 considered to control the mineralization. As with the dominant structure analysis, the results  
525 were normalized against the total fault length of each fault type, and the fault types with very  
526 low counts R'1 and R'2 were removed to prevent skewing of results. A similar set of  
527 analyses for different fault activity timing was performed as for the dominant structure -  
528 scenario, the key results are shown in Fig. 15.

529 Considering only D1 structures within 3 km of a gold occurrence, P1 hosts the highest  
530 number of occurrences per km of fault length, with R1 and Y1 being the next most important  
531 (Fig. 15A). X1 hosts the least occurrences here. but similarly to the dominant structure  
532 analysis becomes more important within the 9 km buffer zone. P1 remains the most

533 important controlling structure within a 9 km radius, although Y1 also remaining a significant  
534 structure. It is noted again that Y1 and P1 have very similar strike.

535 Of the faults formed during D2, X2 emerges as the most significant structure within the 3 km  
536 buffer zone, followed by Y2. Y2 becomes the most significant fault within a 9km buffer zone,  
537 but X2 seems to have importance as well (Fig. 15B). P2 is insignificant within a 3 km zone,  
538 but gains some importance within a 9 km zone, nevertheless being the least important of the  
539 four fault types. Of the reactivated D1 faults (Fig. 15C), P1 is the most important fault,  
540 followed by Y1, with X1 being the least important for both buffer zones. If all faults are  
541 considered, regardless of the timing of their activity (Fig. 15D), within a 3 km radius X2 is the  
542 most significant structure, followed by P1. P2 and X1 are the least important faults. Within a  
543 9 km radius, X2 and P1 maintain their significance, and Y2 remains as an important fault,  
544 but P2 emerges as a significant feature as well, with R1 and R2 being the least important.

#### 545 *6. Discussion*

546 The analysis shows that the majority of gold occurrences occur within c. 3-4 km of a major  
547 fault, and 85% of the deposits that are interpreted to be fault controlled are found within 9km  
548 of a fault (Fig. 13). On the other hand, Fig. 12 shows that gold tends to occur in areas of low  
549 to intermediate fault density. It is likely that faulting below the resolution of our data is  
550 common, and that the damage zones are wider in the vicinity of large faults than in the  
551 vicinity of shorter faults. Consequently, the few large faults can host a large number of  
552 deposits within the sub-resolution structures of their damage zones while at the same time  
553 appearing as a low fault-density area in our regional-scale data. However, there seem to be  
554 no correlation between the fault length and number of gold occurrences per km of fault. Fault  
555 length, therefore, is less important than the fault orientation and fault density in terms of  
556 likelihood of gold occurrence.

557 The 3-4 km distance from any major fault to >50% of gold occurrences is suggested to be  
558 important and a fairly good indicator of whether fault is controlling Au occurrence (Fig. 13B;

559 Table 3; Appendix A). Many faults (P1, Y1, Y2, P2, X2) have a median distance from a gold  
560 occurrence that is around or less than 4 km and also show a significant decrease in  
561 frequency of the occurrences with a distance beyond c. 3-4 km. This is in sharp contrast to  
562 other faults where the gold occurrence frequency seems fairly random (R1, P2, X1, R'1, R'2;  
563 although the last two are very few in total count). This implies that the latter structures may  
564 not directly or only rarely control Au occurrence. P2 or X1 do not emerge as significant Au-  
565 controlling structure within a 3 km buffer zone in the fault type analyses either (Figs. 14 and  
566 15); however, R1 does seem important within a 3 km radius, especially for the 'dominant  
567 structure' scenario (Fig. 15). Gold occurrences assigned to X1 emerge as significant for the  
568 'dominant structure' scenario, but their distance plot shows a relatively even distribution  
569 within c. 9km of these faults, with no clear increase as the fault is approached (Appendix A).  
570 This even spread may indicate that this fault did not in fact control Au deposition, but it is  
571 possible to explain this contradiction by hypothesising that if a large number of X1 faults are  
572 relatively low-angle faults, and if the gold occurrences at the surface occur dominantly in  
573 their hanging-walls, the deposits may be closer to the fault (which would be below the  
574 deposit at depth) than their mutual distance at Earth's surface may suggest. This hypothesis  
575 is supported by the observation that many X1-related Au occurrences are only observed on  
576 one side of their relevant X1 fault, and the trend of these Au occurrences tend to be linear  
577 along the fault strike and apparently unaffected by other structures. Indeed, X1 strike  
578 approximately coincides with the orientation of the interpreted SE-verging thrust faults in  
579 Côte d'Ivoire (e.g. Eisenlohr and Hirdes, 1992).

580 The fault type analyses (Figs. 14 and 15) for the dominant and the proximal structures show  
581 some differences. For the dominant structure, Y2 is the most important fault within a 3 km  
582 buffer zone, followed closely by Y1 and R1. For the proximal structures, X2 and P1 are the  
583 most significant faults, followed by Y2. X2 with Au within a 15 km radius has a relatively low  
584 total count (n = 17; Appendix A) and has not to our knowledge been described in literature;  
585 therefore the real significance of this fault type remains speculative. Based on the discussion

586 above on the distribution pattern of Au away from faults, we suggest that the proximal  
587 structures are more likely to control Au occurrence than fault length i.e. dominant structure.  
588 This interpretation would mean that, excluding X2, P1 and Y2 would be the most significant  
589 faults for Au occurrence. Therefore, a dominantly NE-SW trending pattern is revealed to host  
590 the majority of the gold deposits, although the c. N-S and ENE-WSW trends are also  
591 important.

592 It is uncertain why the P2, while concordant with the NE-SW main trend, does not show  
593 significant mineralization. We tentatively hypothesise that this may be due to the very similar  
594 trend of P2 with that of P1: continuing or renewed deformation is more likely to localize along  
595 an already existing long weakness zones rather than along a completely new fault zone (e.g.  
596 Sibson, 1985). If fault and fracture connectivity and, therefore, fluid conduits were already  
597 well established along P1 structures and their damage zones, it is likely that these pre-  
598 existing conduits were preferentially exploited by later mineralizing fluids as well. Formation  
599 of P2 faults seems to indeed have been a fairly rare event: there are only 33 interpreted P2  
600 faults whereas the number of P1 faults total 150 (Table 3). P2 faults are also 20% shorter  
601 than P1 faults, therefore probably carrying less displacement and narrower damage zones  
602 which may imply that they were less likely to link to fluid pathways. On the other hand, P2  
603 strike is relatively close to that of Y2, and it is possible that some of either Y2 or P2 faults  
604 have been mis-assigned accordingly. These faults, however, are relatively straight, reflected  
605 in their low circular variance. This helps in deciding to which Riedel category each fault  
606 belongs. The fact that the lack of Au association with P2 is a systematic and a very distinct  
607 pattern also suggests that this is a real feature and not a result of mis-assignment of faults.

608 The detailed timing of the orogenic gold mineralization in Côte d'Ivoire and the equivalent  
609 Birimian terranes in neighbouring countries has been somewhat debated but it is generally  
610 agreed that the onset of gold mineralisation occurred during late Eburnean Orogeny  
611 approximately 2.1-2.0 Ga (e.g. Milési et al., 1991, 1992; Pigois et al., 2003; Béziat et al.,  
612 2008; Camus et al., 2008; Markwitz et al., 2016; Augustin et al., 2017). A second

613 mineralization phase has also been suggested soon after the main Eburnean phase (e.g.  
614 Milési et al., 1992; Camus et al., 2008; Traoré et al., 2016). Especially the importance,  
615 extent, and timing of this later event is debated. Many authors allocate the peak  
616 mineralization to the c. 2.15-2.1 Ma time interval (i.e. our D1; e.g. Markwitz et al., 2016)  
617 while others suggest that, at least locally, the younger, post-2.1 Ma event was equally or  
618 more important (i.e. our D2; e.g. Pigois et al., 2003; Chudasama et al., 2016; Traoré et al.,  
619 2016; Le Mignot et al., 2017). Our analysis results indicate strong and systematic correlation  
620 between Au and both D1 and D2 structures in Côte d'Ivoire. This implies that mineralisation  
621 occurred during both phases of deformation. However, when all existing structures are  
622 considered, there is a strong influence from the D2 data. This may be interpreted as peak  
623 mineralisation occurring during D2 at a regional scale, albeit sometimes utilizing reactivated  
624 D1 structures (especially P1). Locality-specific peak mineralization may naturally show  
625 deviations of this regional trend and have occurred in either D1 or D2 (e.g. Markwitz et al.,  
626 2016; Traoré et al., 2016). Reports do exist of the strong control of the D2 faulting, including  
627 reactivation of D1 structures, of gold deposition in the Birimian: e.g. Chudasama et al. (2016)  
628 discuss the reactivation of the D1 NE-SW striking thrusts during D2 in the Kumasi Basin in  
629 Ghana.

630 Berge (2011) suggests that the deformation event with a NW-SE stress field was  
631 compressional and semi-ductile while the later c. NE-SW stress field caused transpressional  
632 and mostly brittle deformation. The transpressional and more brittle nature of D2 may  
633 theoretically have caused more dilational (i.e. locally extensional) sites to form to allow fluid  
634 flow and peak mineralization. However, according to Augustin et al. (2017) D1 was also  
635 transpressional with progressively from c. ENE-SSW to NNW-SSE rotating compression;  
636 this is in our opinion likely given the commonly transpressional nature of most orogenic  
637 systems. Obviously, the mineralizing fluid flow needs to coincide with the formation of  
638 suitable transport structures connected to the fluid source(s), and the formation of suitable  
639 trap/deposition sites. In purely structural terms, there seems to be no significant difference

640 between the structural style of deformation between D1 and D2, although D2 faulting may  
641 well have increased the connectivity of the fault network and, as such, eased the fluid  
642 transport. The possible peak mineralization during D2 could therefore either reflect the  
643 higher connectivity of large-scale faults, or simply the availability of the gold-bearing fluids  
644 controlled by larger-scale hydrothermal evolution of this part of the crust.

645 As a final note, although the structures are likely to form the first-order control on the  
646 orogenic gold mineralization, one should not forget the role of lithological changes. In terms  
647 of the main lithologies in Côte d'Ivoire, the volcano-sedimentary rocks are the dominant  
648 hosts when all potentially structurally controlled gold occurrences are considered (Au per  
649 km<sup>2</sup>; Fig. 10A). However, a more detailed analysis shows that those gold occurrences that  
650 are most likely to be structurally controlled (i.e. within c. 3km of a fault, Au per km of fault  
651 length; Fig. 10B) are more equally distributed between the three main rock units, although  
652 the volcanoclastics are still the dominant lithology. In the Birimian, the late- and post-  
653 Eburnean shear zones and the orogenic gold deposits controlled by them typically occur at  
654 the contact between the Birimian metasediments and metavolcanics (e.g. Markwitz et al.,  
655 2016). This is unsurprising as a lithological boundary is also likely to be a rheological  
656 boundary, causing strain partitioning into a shear zone. This is also the case in our analysis  
657 as many of the gold-hosting faults are seen to have localized near or at major lithological  
658 contacts. It may be that gold deposition close to these boundaries is also enhanced by  
659 chemical and physical changes at lithological contacts. For example, within the Birimian  
660 greenstones, the volcano-sediments host slightly more occurrences than the turbidites within  
661 3km of a fault. The reasons for this is unclear and would require further study, but it may be  
662 a result of differences in e.g. porosity, permeability, and/or geochemistry of the trapping  
663 lithology. One fairly simple scenario might be that, if the metavolcanics show higher  
664 competence than the metaturbidites, they will deform in a more brittle manner which will  
665 enhance fracturing. A similar behaviour has been suggested for e.g. the Ashanti Belt in

666 Ghana, where the gold is principally hosted within a metabasaltic unit exhibiting more  
667 competent behaviour than the surrounding metasediments (Perrouty et al., 2014).

668

669 *Acknowledgements*

670 Sincere thanks to ToroGold for providing the data for the MSc Structural Geology with  
671 Geophysics dissertation project by SM onto which this paper is based. This research did not  
672 receive any specific grant from funding agencies in the public, commercial, or not-for-profit  
673 sectors. The reviewers Lenka Baratoux, Mark Jessell, and Anonymous are thanked for the  
674 thorough and useful comments; many thanks also to the journal editor Damien Delvaux.

675 *References*

- 676 Allibone, A., Teasdale, J., Cameron, G., Etheridge, M., Uttley, P., Soboh, A., Appiah-Kubi, J.,  
677 Adanu, A., Arthur, R., Mamphey, J., Odoom, B., Zuta, J., Tsikata, A., Pataye, F., Famiyeh, S.,  
678 2002. Timing and structural controls on gold mineralisation at the Bogoso Gold Mine, Ghana,  
679 West Africa. *Econ. Geol.* 97, 949–969.
- 680 Augustin, J., Gaboury, D., Crevier, M., 2017. Structural and gold mineralizing evolution of the  
681 world-class orogenic Mana district, Burkina Faso: Multiple mineralizing events over 150  
682 million years. *Ore Geol. Reviews* 91, 981-1012.
- 683 Bagarre, E., Tagini, B., 1965. Carte Géologique de la Côte d'Ivoire 1:1 000 000. Abidjan: La  
684 Direction des Mines et de la Géologie du Gouvernement de la Côte d'Ivoire.
- 685 Ballo, I., Hein, K.A.A., Guindo, B., Sanogo, L., Ouologuem, Y., Daou, G., Traoré, A. 2016.  
686 The Syama and Tabakoroni goldfields, Mali. *Ore Geol. Reviews* 78, 578-585.
- 687 Baratoux, L., Metelka, V., Naba, S., Jessell, M.W., Gregoire, M., Ganne, J., 2011. Juvenile  
688 Paleoproterozoic crust evolution during the Eburnean orogeny (~2.2-2.0 Ga), western  
689 Burkina Faso. *Prec. Res.* 191, 18-45.
- 690 Baratoux, L., Metelka, V., Naba, S., Ouyi, P., Siebenaller, L., Jessell, M.W., Naré, A., Salvi,  
691 S., Béziat, D., Franceschi, G., 2015. Tectonic evolution of the Gaoua region, Burkina Faso:  
692 Implications for mineralization. *J. Afr. Earth Sci.* 112, 419-439.
- 693 Berge, J., 2011. Paleoproterozoic, turbidite-hosted, gold deposits of the Ashanti gold belt  
694 (Ghana, West Africa): Comparative analysis of turbidite-hosted gold deposits and an  
695 updated genetic model. *Ore Geol. Reviews* 39, 91-100.
- 696 Béziat, D., Dubois, M., Debat, P., Nikiéma, S., Salvi, S., Tollon, F., 2008. Gold metallogeny  
697 in the Birimian craton of Burkina Faso (West Africa). *J. Afr. Earth Sci.* 50, 215–233.
- 698 Block, S., Ganne, J., Baratoux, L., Zeh, A., Parra-Avila, L.A., Jessell, M., Ailleres, L.,  
699 Siebenaller, L., 2015. Petrological and geochronological constraints on lower crust  
700 exhumation during Paleoproterozoic (Eburnean) orogeny, NW Ghana, West African Craton.  
701 *J. Metam. Geol.* 33, 463-494.
- 702 Camus, Y., Rousseau, G., Gagnon, G., Duplessis, C., 2008. Technical Report: Preliminary  
703 feasibility study and certification of reserves of the Ity mine - Ivory Coast. Québec: Geostat  
704 Systems International Inc for La Mancha Resources Inc.
- 705 <https://www.endeavourmining.com/document-library/default.aspx>; accessed 25 August 2018.

706 Cartwright, J.A., Mansfield, C., Trudgill, B., 1996. The growth of normal faults by segment  
707 linkage. *Geol. Soc., London, Spec. Publ.* 99,163–177.

708 Chudasama, B., Porwal, A., Kreuzer, O.P., Butera, K., 2016. Geology, geodynamics and  
709 orogenic gold prospectivity modelling of the Paleoproterozoic Kumasi Basin, Ghana, West  
710 Africa. *Ore Geology Reviews* 78, 692-711.

711 Coulibaly, Y., Boiron, M.C., Cathelineau, M., Kouamelan, A.N., 2008. Fluid immiscibility and  
712 gold deposition in the Birimian quartz veins of the Angovia deposit (Yaouré, Ivory Coast). *J.*  
713 *Afr. Earth Sci.* 50, 234–254.

714 Cox, S.F., 1999. Deformational controls on the dynamics of fluid flow in mesothermal gold  
715 systems. In: McCaffrey, K.J.W., Lonergan, L., Wilkinson, J.J. (eds.) *Fractures, Fluid Flow*  
716 *and Mineralization*. *Geol. Soc., London, Spec. Publ.* 155,123–140.

717 Criddle, P., Marissen, C., Quartermaine, J., de la Mare, G., 2011. Form 43-101 Technical  
718 Report: Central Ashanti Gold Project, Ghana - Perseus Mining Limited.  
719 [http://www.perseusmining.com/technical\\_reports.60.html](http://www.perseusmining.com/technical_reports.60.html); accessed 25 August 2018.

720 Delor, C., Yao, B.D., 1998. Carte Géologique Provisoire de la Côte d'Ivoire a 1/200 000.  
721 Abidjan: Direction des mines et de la géologie de Côte d'Ivoire.

722 Eisenlohr, B.N., Hirdes, W., 1992. The structural development of the early Proterozoic  
723 Birimian and Tarkwaian rocks of southwest Ghana, West Africa. *J. Afr. Earth Sci.* 14, 313-  
724 325.

725 Esri 2015. ArcGIS 10.3.1 for Desktop.

726 Esri 2016b. How Line Density Works: ArcMap 10.3.

727 Esri 2016c. How Linear Directional Mean works: ArcMap 10.3.

728 Fossen, H., 2010. *Structural Geology*. Cambridge University Press. 463 p.

729 Goldfarb, R.J., Baker, T., Dubé, B., Groves, D.I., Hart, C.J.R., Gosselin, P., 2005.  
730 Distribution, character, and genesis of gold deposits in metamorphic terranes. In:  
731 Hedenquist, J.W., Thompson, J.F.H., Goldfarb, R.G., Richards, J.P., (eds.) *Economic*  
732 *geology 100th Anniversary volume*, *Soc. Econ. Geol.*, 407-450.

733 Groves, D.I., Goldfarb, R.J., Knox-Robinson, C.M., Ojala, J., Gardoll, S., Yun, G.Y.,  
734 Holyland, P., 2000. Late-kinematic timing of orogenic gold deposits and significance for  
735 computer-based exploration techniques with emphasis on the Yilgarn Block, Western  
736 Australia. *Ore Geo. Reviews* 17,1–38.

737 Hirdes, W., Davis, D.W., Lütke, G., Kinan G., 1996. Two generations of Birimian  
738 (Paleoproterozoic) volcanic belts in northeastern Côte d'Ivoire (West Africa): consequences  
739 for the 'Birimian controversy'. *Prec. Res.* 80, 173-191.

740 Hagemann, S.G., Cassidy, K., 2000. Archean orogenic lode gold deposits. *SEG Reviews* 13,  
741 9–68.

742 Jessell, M.W., Amponsah, P.O., Baratoux, L., Asiedu, D.K., Loh, G.K., Ganne, J., 2012.  
743 Crustal-scale transcurrent shearing in the Paleoproterozoic Sefqi-Sunyani-Comoé region,  
744 West Africa. *Prec. Res.* 212-213, 155-168.

745 Jessell, M., Santoul, J., Baratoux, L., Youbi, N., Ernst, R.E., Metelka, V., Miller, J., Perrouty,  
746 S., 2015. An updated map of West African mafic dykes. *J. Afr. Earth Sci.* 112, 440-450.

747 John, T., Klemd, R., Hirdes, W., Loh, G., 1999. The metamorphic evolution of the  
748 Paleoproterozoic (Birimian) volcanic Ashanti belt (Ghana, West Africa). *Prec. Res.* 98, 11–  
749 30.

750 Johnson, N., de Klerk, Q., Yeo, W., Roux, A., 2013. Technical Report and Mineral Resource  
751 and Reserve Update for the Nzema Gold Mine, Ghana, West Africa. Grand Cayman:  
752 Endeavor Mining Corporation.  
753 [https://s21.q4cdn.com/954147562/files/doc\\_downloads/technical\\_report/lan-Hamilton-](https://s21.q4cdn.com/954147562/files/doc_downloads/technical_report/lan-Hamilton-technical-report-nzema.pdf)  
754 [technical-report-nzema.pdf](https://s21.q4cdn.com/954147562/files/doc_downloads/technical_report/lan-Hamilton-technical-report-nzema.pdf) accessed 18 December 2018.

755 Le Mignot, E., Reisberg, L., André-Mayer, A-S., Bourassa, Y., Fontaine, A., Miller, J., 2017.  
756 Re-Os geochronological evidence for multiple Paleoproterozoic gold events at the scale of  
757 the West African Craton. *Economic Geology* 112, 145-168.

758 Lompo, M., 2010. Paleoproterozoic structural evolution of the Man-Leo Shield (West Africa).  
759 Key structures for vertical to transcurrent tectonics. *J. Afr. Earth Sci.* 58, 19–36.

760 de la Mare, G., 2010. Form 43-101, Technical Report: Tengrela Gold Project, Ivory Coast -  
761 Perseus Mining Limited. [http://www.perseusmining.com/technical\\_reports.60.html](http://www.perseusmining.com/technical_reports.60.html), accessed  
762 25 August 2018.

763 Marcoux, E., Milési, J.P., 1993. Lead isotope signature of Early Proterozoic ore deposits in  
764 western Africa: Comparison with gold deposits in French Guiana. *Econ. Geology* 88, 1862–  
765 1879.

766 Markwitz, V., Hein, K.A.A., Miller, J., 2016. Compilation of West African mineral deposits:  
767 Spatial distribution and mineral endowment. *Prec. Res.* 274, 61-81.

- 768 Marshak, S. 1999. Deformation style way back when: Thoughts on the contrasts between  
769 Archean/Paleoproterozoic and contemporary orogens. *J. Struct. Geol.* 21, 1175–1182.
- 770 McFarlane, C.R.M., Mavrogenes, J., Lentz, D., King, K., Allibone, A., Holcombe, R., 2011.  
771 Geology and intrusion-related affinity of the Morila gold mine, Southeast Mali. *Econ. Geol.*  
772 106, 727-750.
- 773 Metelka, V., Baratoux, L., Naba, S., Jessell, M.W., 2011. A geophysically constrained litho-  
774 structural analysis of the Eburnean greenstone belts and associated granitoid domains,  
775 Burkina Faso, West Africa. *Prec. Res.* 190, 48-69.
- 776 Milési, J.P., Ledru, P., Ankrah, P., Johan, V., Marcoux, E., Vinchon, C., 1991. The  
777 metallogenic relationship between Birimian and Tarkwaian gold deposits in Ghana.  
778 *Mineralium Deposita* 26, 228–238.
- 779 Milési, J.P., Ledru, P., Feybesse, J.L., Dommange, A., Marcoux, E. 1992. Early Proterozoic  
780 ore deposits and tectonics of the Birimian orogenic belt, West Africa. *Prec. Res.* 58, 305–  
781 344.
- 782 Nyame, F.K., 2013. Origins of Birimian (ca 2.2 Ga) mafic magmatism and the  
783 Paleoproterozoic 'greenstone belt' metallogeny: a review. *Island Arc* 22, 538–548.
- 784 Parra-Avila, L.A., Bourassa, Y., Miller, J., Perrouy, S., Fiorentini, M.L., McCuaig, T.C., 2015.  
785 Age constraints of the Wassa and Benso mesothermal gold deposits, Ashanti Belt, Ghana,  
786 West Africa. *J. Afr. Earth Sci.* 112, 524-535.
- 787 Peacock, D.C.P., Sanderson, D.J., 1991. Displacement, segment linkage and relay ramps in  
788 normal fault zones. *J. Struct. Geol.* 13, 721–733.
- 789 Perrouy, S., Lindsay, M.D., Jessell, M.W., Aillères, L., Martin, R., Bourassa, Y., 2014. 3D  
790 modeling of the Ashanti Belt, southwest Ghana: Evidence for a litho-stratigraphic control on  
791 gold occurrences within the Birimian Sefwi Group. *Ore Geology Reviews* 63, 252-264.
- 792 Pigois, J.P., Groves, D.I., Fletcher, I.R., McNaughton, N.J., Snee, L.W., 2003. Age  
793 constraints on Tarkwaian palaeoplacer and lode-gold formation in the Tarkwa-Damang  
794 district, SW Ghana. *Miner. Dep.* 38, 695-714.
- 795 Pitra, P., Kouamelan, A.N., Ballèvre, M., Peucat, J-J., 2010. Palaeoproterozoic high-  
796 pressure granulite overprint of the Archaean continental crust: evidence for homogeneous  
797 crustal thickening (Man Rise, Ivory coast). *J. Metam. Geol.* 28, 41-58.
- 798 Sibson, R.H., 1985. A note on fault reactivation. *J. Struct. Geol.* 7, 751–754.

799 Sibson, R.H., Robert, F., Poulsen, K.H., 1988. High-angle reverse faults, fluid-pressure  
800 cycling, and mesothermal gold-quartz deposits. *Geology* 16, 551-555.

801 Traoré, Y.D., Siebenaller, L., Salvi, S., Béziat, D., Bouaré, M.L., 2016. Progressive gold  
802 mineralization along the Syama corridor, southern Mali (West Africa). *Ore Geol. Reviews*,  
803 78, 586-598.

804 Vidal, M., Alric, G., 1994. The Palaeoproterozoic (Birimian) of Haute-Comoé in the West  
805 African craton, Ivory Coast: a transtensional back-arc basin. *Prec. Res.* 65, 207–229.

806 Vidal, M., Gumiaux, C., Cagnard, F., Pouclet, A., Ouattara, G., Pichon, M. 2009. Evolution of  
807 a Paleoproterozoic ‘weak type’ orogeny in the West African Craton (Ivory Coast).  
808 *Tectonophysics* 477, 145–159.

809 Viola, G., Odonne, F., Mancktelow, N.S., 2004. Analogue modelling of reverse fault  
810 reactivation in strike-slip and transpressive regimes: application to the Giudicarie fault  
811 system, Italian Eastern Alps. *J. Struct. Geol.* 36, 401-418.

812 Waller, C.G., Thompson, P.W., Brammer, S., McDiarmid, J., Lane, C., 2015. Sissingué gold  
813 project, Côte d’Ivoire: National Instrument 43-101 Technical Report. Lycopodium Minerals  
814 Pty Ltd for Perseus Mining Ltd. [http://www.perseusmining.com/technical\\_reports.60.html](http://www.perseusmining.com/technical_reports.60.html);  
815 accessed 25 August 2018.

816 Walsh, J.J., Watterson, J., 1988. Analysis of the relationship between displacements and  
817 dimensions of faults. *J. Struct. Geol.* 10, 239-247.

818 Walsh, J.J., Watterson, J., Heath, A., Gillespie, P.A., Childs, C., 1998. Assessment of the  
819 effects of sub-seismic faults on bulk permeabilities of reservoir sequences. *Geol. Soc.*,  
820 London, Spec. Publ. 127, 99-114.

821 Woodcock, N.H., Fischer, M., 1986. Strike-slip duplexes. *J. Struct. Geol.* 8, 725-735.

822 Xu, S. and Ben-Zion, Y. 2013. Numerical and theoretical analyses of in-plane dynamic  
823 rupture on a frictional interface and off-fault yielding patterns at different scale. *Geophysical*  
824 *Journal International.* 193(1),pp.304–320.

825 Figure captions

826 Fig. 1. Simplified geological map of Côte d'Ivoire. Adapted from Bagarre and Tagini (1965);  
827 base map by Esri (2015).

828 Fig. 2. A schematic representation of the role of a pre-existing fault where  $\theta$  is the angle of  
829 the fault relative to  $\sigma_1$ . The shaded area represents the range of  $2\theta$  where the fault may be  
830 reactivated. Based on Fossen (2010).

831 Fig. 3. An example of a fault network showing typical locations of Au mineralization (red  
832 dots). Locations include: a) fault jogs and b) bends; c) fault intersections; d) lithological  
833 boundaries (dashed); and minor faults such as e) dangling structures where fluids (red  
834 arrows) may become trapped.

835 Fig. 4. Spatial extent of the A) geophysical data, and B) 1:200,000 - 1:500,000 geological  
836 maps used in the fault interpretation.

837 Fig. 5. Relationship between lithology, faults (with the last interpreted kinematic activity), and  
838 gold. Note that the indicated kinematics does not reflect the presence of any dip-slip  
839 component; for example. at least some of the c. NE-SW striking faults have a significant  
840 reverse/thrust component (Eisenlohr and Hirdes, 1992). This has, however, been accounted  
841 for in the models and the analyses (see text).

842 Fig. 6. Examples of fault interpretation from geophysical data. A) A sinistral Y1 fault identified  
843 by deflection of the magnetic fabric (in the centre; an short segment of a related fault on the  
844 right shows dextral kinematics due to its location in an extensional jog); B) This linear feature  
845 coincides with a probable dyke (Jessell et al., 2015) but around it asymmetric fabrics are  
846 identified in the TMI, therefore we interpret that the dyke intruded along a sinistral R'2 fault  
847 (many but not all dykes were interpreted to intrude along faults); C) A dextral Y2 fault  
848 identified by sigmoidal lows; D) A possible reactivated D1 fault: the orientation matches the  
849 dextral Y1 fault trend but the sigmoidal lows indicate sinistral reactivation under  $\sigma_1^B$  during  
850 D2.

851 Fig. 7. A) All fault interpretations colour-coded according to their assigned Riedel structure.  
852 B) Summary Riedel models with the approximate orientation of the maximum principal stress  
853  $\sigma_1$  indicated. R, Y, and P are synthetic shear fault orientations with Y also being the  
854 theoretical main displacement surface; R' is the main antithetic shear fault orientation; X is  
855 the reverse or thrust fault orientation (illustrated with triangles on the fault line). M<sup>I</sup> = An  
856 idealized Riedel model where  $\sigma_1$  bisects the angle between R and R'1 (dashed line); M<sup>A</sup> =  
857 model for D1; M<sup>B</sup> = model for D2. Note that for R1 faults in M<sup>A</sup>, the model reflects the  
858 dominant strikes of the main body of R1 faults and not the mean strike of c. 21° (Table 3): the  
859 mean strike is interpreted to have been skewed by the abundant NE-SW striking horse-tail  
860 splays and curved fault tips associated with this fault type (see also Fig. 8).

861 Fig. 8. Mean fault strike variations split by lithology. Note that this figure illustrates the strike  
862 variability only; the various strikes are not weighed according to the total fault length in each  
863 strike direction. See e.g. Fig. 7 for the Riedel geometries revealed by the map patterns.

864 Fig. 9. D1 and D2 fault properties plots based on Table 3. See text for discussion. A) Total  
865 count of faults vs. mean length of D1 faults; B) Total count of faults vs. mean length of D2  
866 faults; C) Angle between mean fault strike and  $\sigma_1^A$  vs. total count of D1 faults; D) Angle  
867 between mean fault strike and  $\sigma_1^B$  vs. total count of D2 faults; E) Percentage of D1 faults re-  
868 activated during D2 vs. angle between mean D1 fault strike and  $\sigma_1^B$ .

869 Fig. 10. A) Number of gold occurrences per km<sup>2</sup> of each lithology with disproportionately  
870 small classes removed; all gold occurrences within 15 km of any fault; B and C) Number of  
871 gold occurrences per km of a fault within each lithology, within B) 3km of a fault; and C)  
872 within 9 km of a fault.

873 Fig. 11. A) Fault density map (non-length weighted) with known gold occurrences; B)  
874 Distribution plot of Au occurrences vs. fault density.

875 Fig. 12. A) Fault density map (length weighted) with known gold occurrences; B) Distribution  
876 plot of Au occurrences vs. fault density. Length-weighting the fault density maps shifts both

877 the median and the 85% cut-off for Au towards the lower-density end of the plot, compared  
878 to Fig. 11. See text for discussion.

879 Fig. 13. Key distribution graphs of the distance between Au and nearest fault (not total  
880 length-weighted). A) All faults and all Au occurrences. The median and 85% values are  
881 shown for all Au occurrences ( $n_{Au} = 909$ ), and for the Au occurrences that occur within the  
882 85% value of all gold occurrences and are therefore interpreted to possibly be fault  
883 controlled ( $n_{Au}^* = 769$ ): see text; B) An example of a distance-variable distribution of Au  
884 occurrences (with near-logarithmic decrease of Au frequency with distance). In this case, the  
885 median for Au for Y2 fault is 2.5 km, with the Au occurrence frequency rapidly decreasing  
886 with larger distance from the fault. This distribution is interpreted to be a strong implication  
887 that this fault type controls Au occurrence. C) An example of a random distribution of Au with  
888 distance from a fault. In this case, the median for Au near P2 faults is not anomalously high  
889 but the Au occurrence frequency does not decrease significantly with distance. This is  
890 interpreted to imply that this fault type may not control significant Au. See Appendix A for all  
891 distribution plots for faults within 15 km of an Au occurrence.

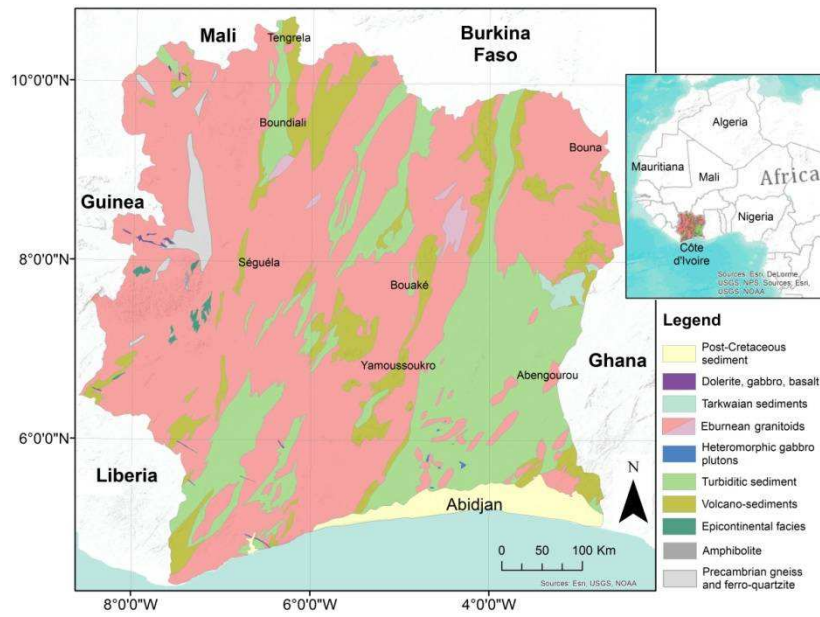
892 Fig. 14. Graphs showing the relationships between Au, the dominant structure (i.e. with a  
893 greatest length within a neighbourhood), and deformation phases, each within 3 km and 9  
894 km neighbourhood radii (left-hand column and right-hand column, respectively). Each graph  
895 is also illustrated with a rose plot, note the different scales in the rose plot. All results are  
896 normalized against total length for each structure, giving the number of Au deposits per km  
897 of each fault type within the 3 km or 9 km neighbourhood. A) Dominant D1 structures during  
898 D1; B) Dominant D2 structures during D2; C) Dominant structures from all D1 faults that are  
899 interpreted to have reactivated during D2; D) Dominant structures from all structures.

900 Fig. 15. Graphs showing the relationships between Au, the proximal structure (i.e. nearest  
901 structure to a deposit), and deformation phases, each within 3 km and 9 km neighbourhood  
902 radii (left-hand column and right-hand column, respectively). Each graph is also illustrated  
903 with a rose plot. All results are normalized against total length for each structure. A) Proximal

904 D1 structures during D1; B) Proximal D2 structures during D2; C) Proximal structures from  
905 all D1 faults that are interpreted to have reactivated during D2; D) Proximal structures from  
906 all structures.

907

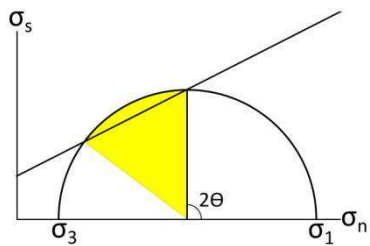
908 Figure 1



909

910

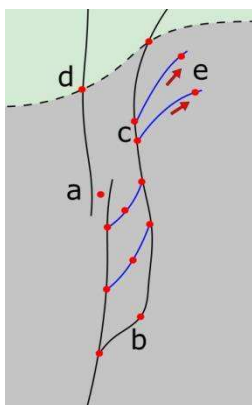
911 Figure 2



912

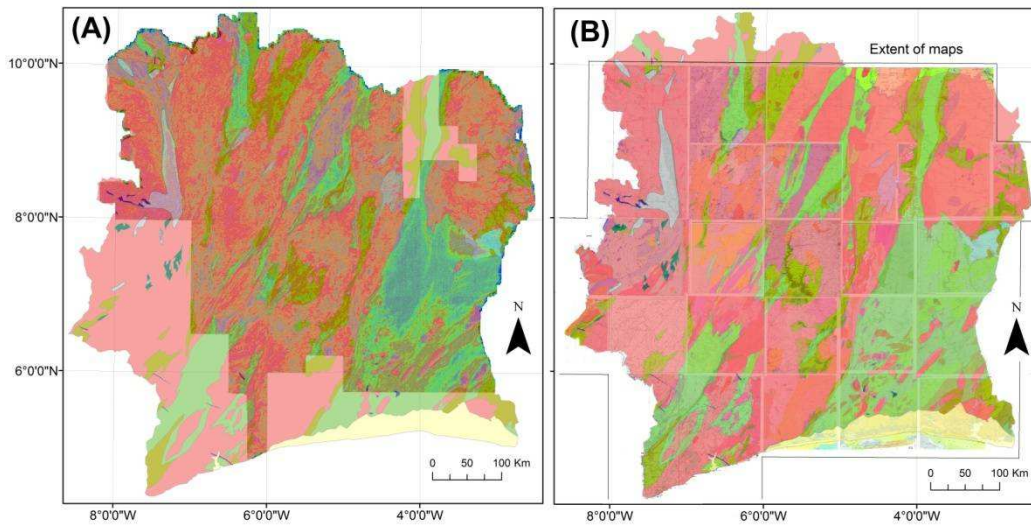
913

914 Figure 3



915

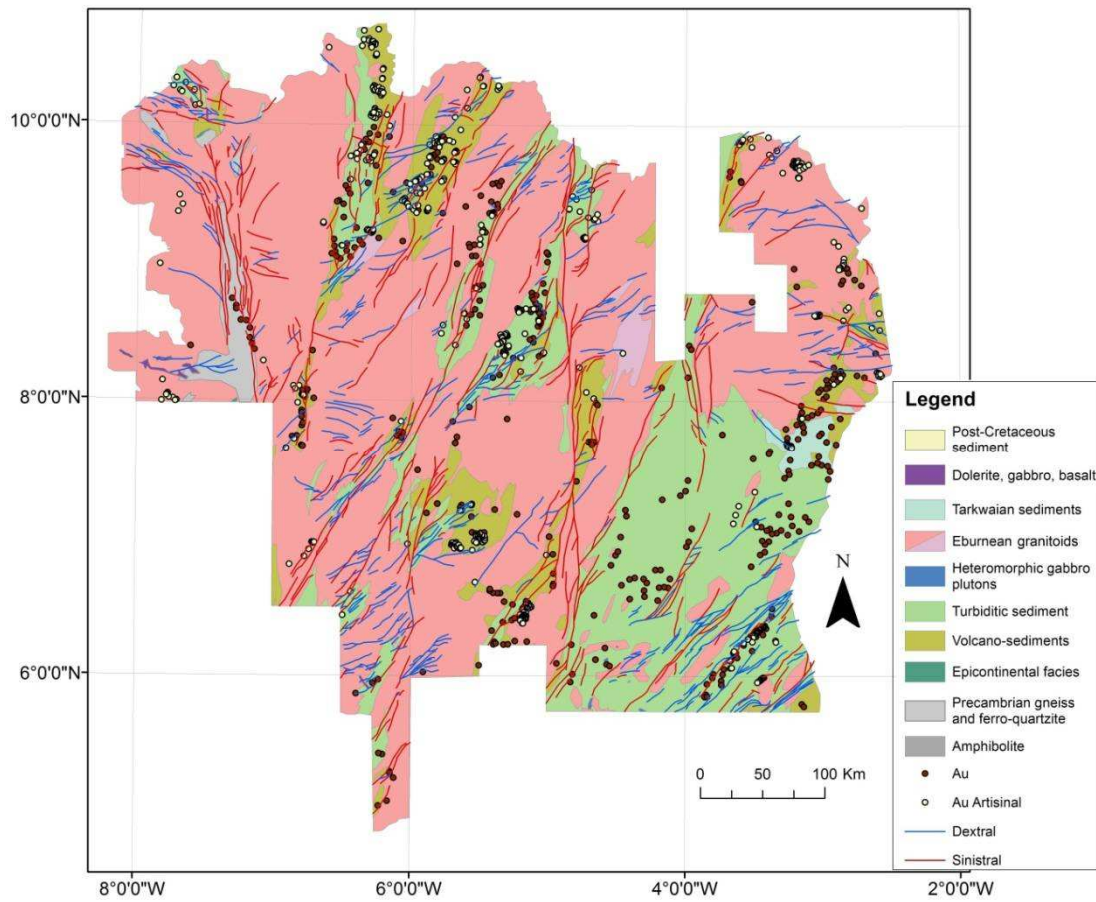
916 Figure 4



917

918

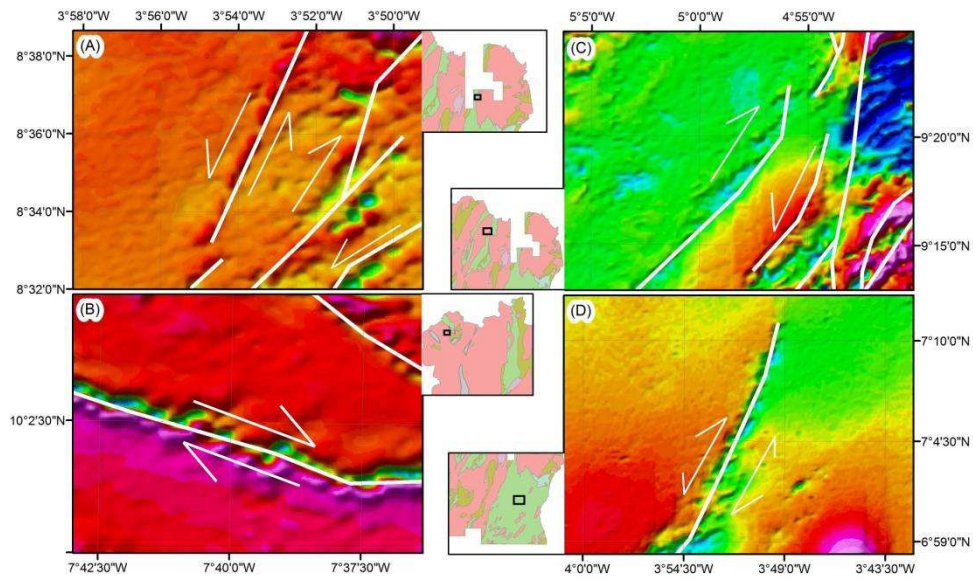
919 Figure 5



920

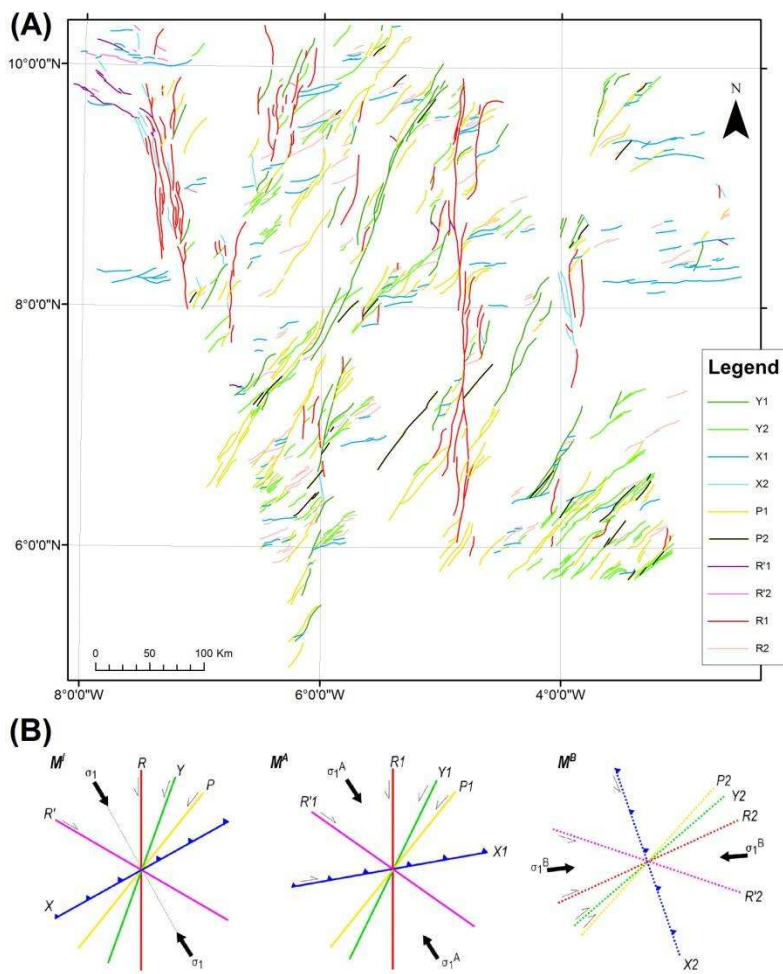
921

922 Figure 6



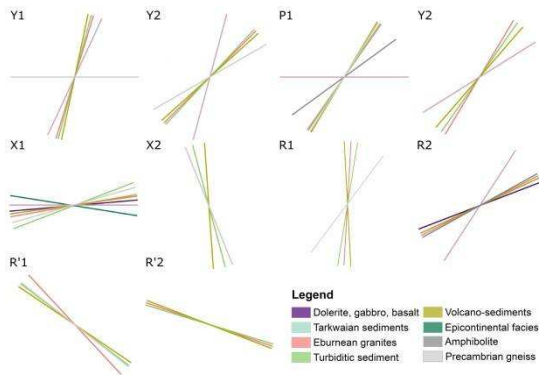
923

924 Figure 7



925

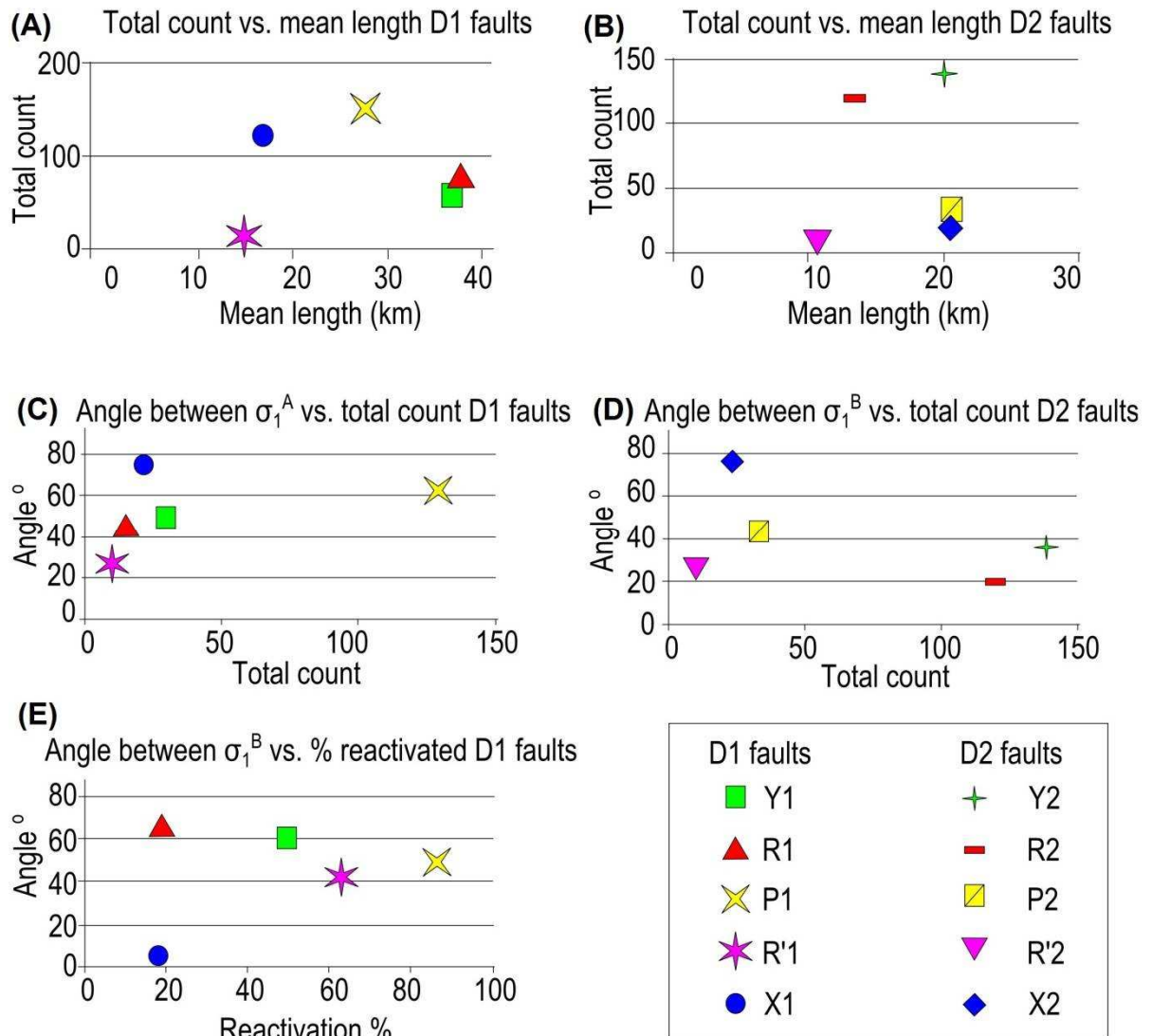
926 Figure 8



927

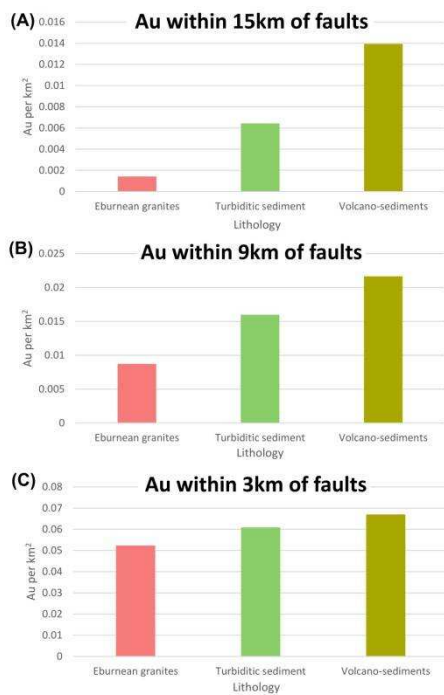
928

929 Figure 9



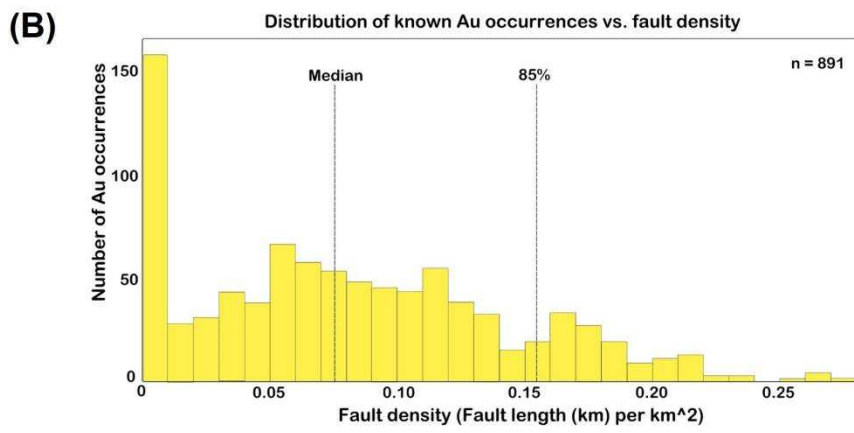
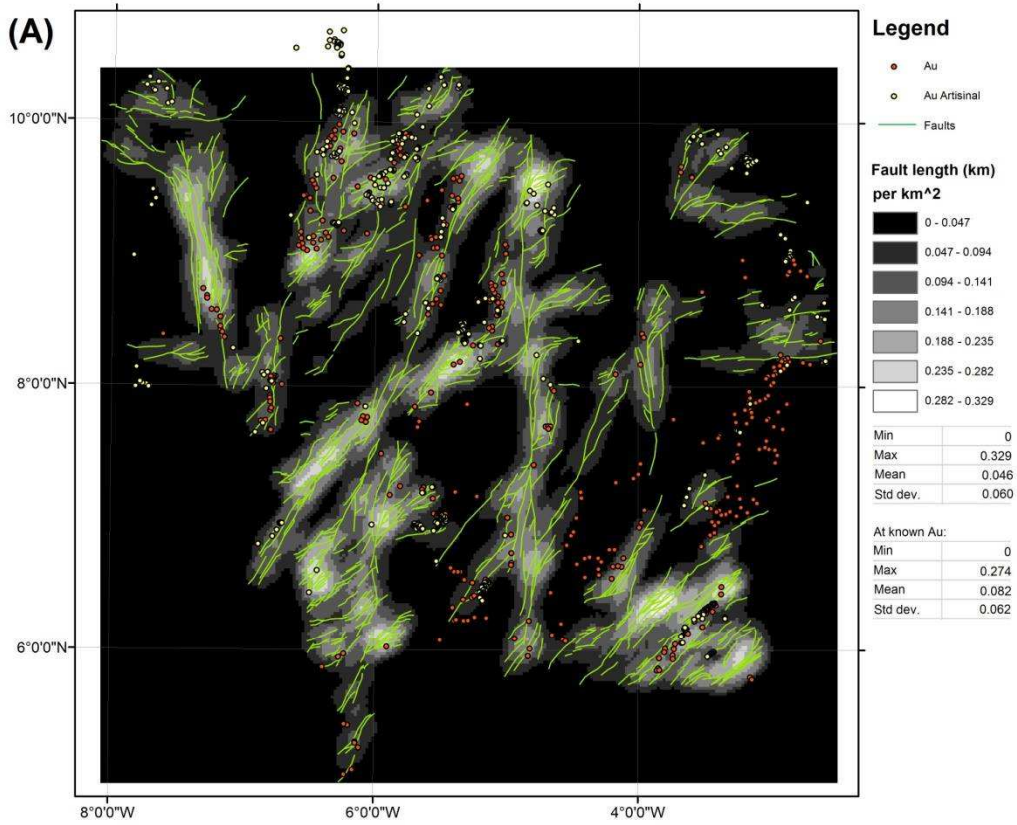
930

931 Figure 10



932

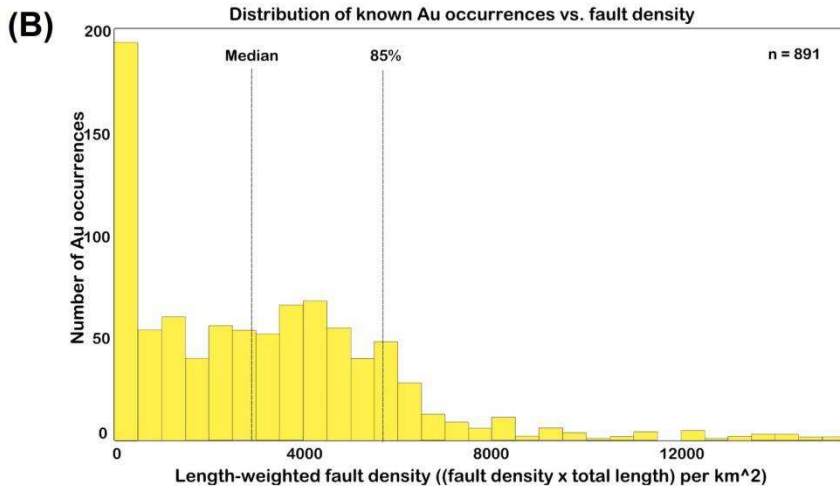
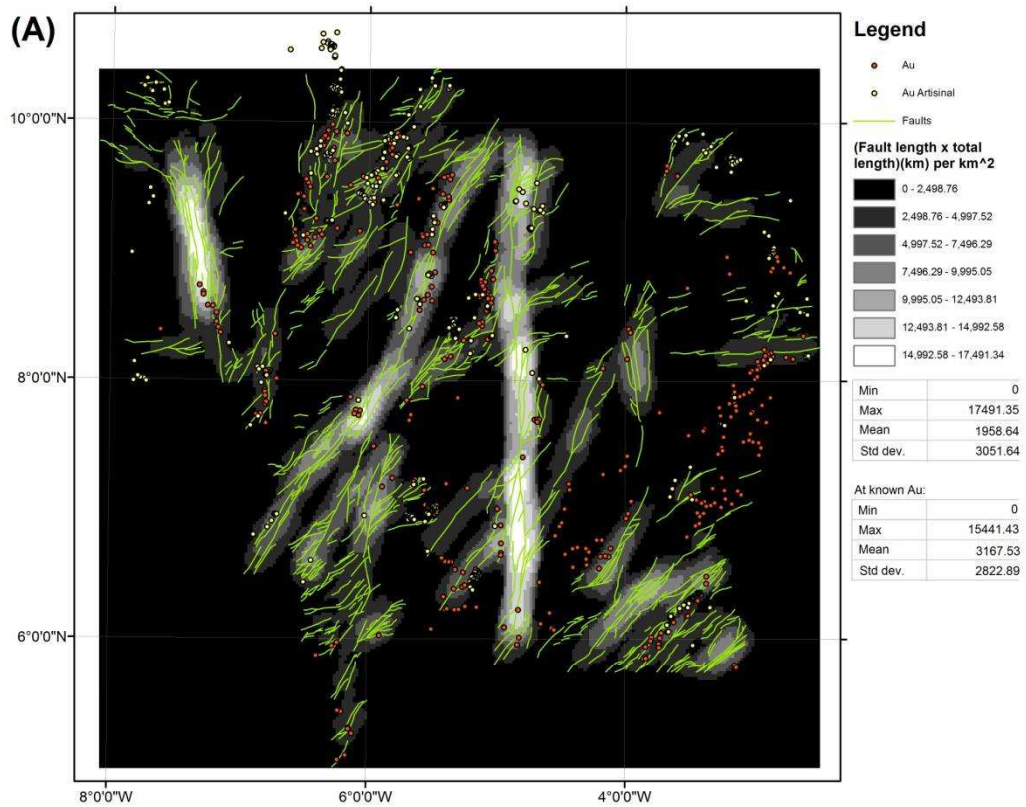
933



935

936

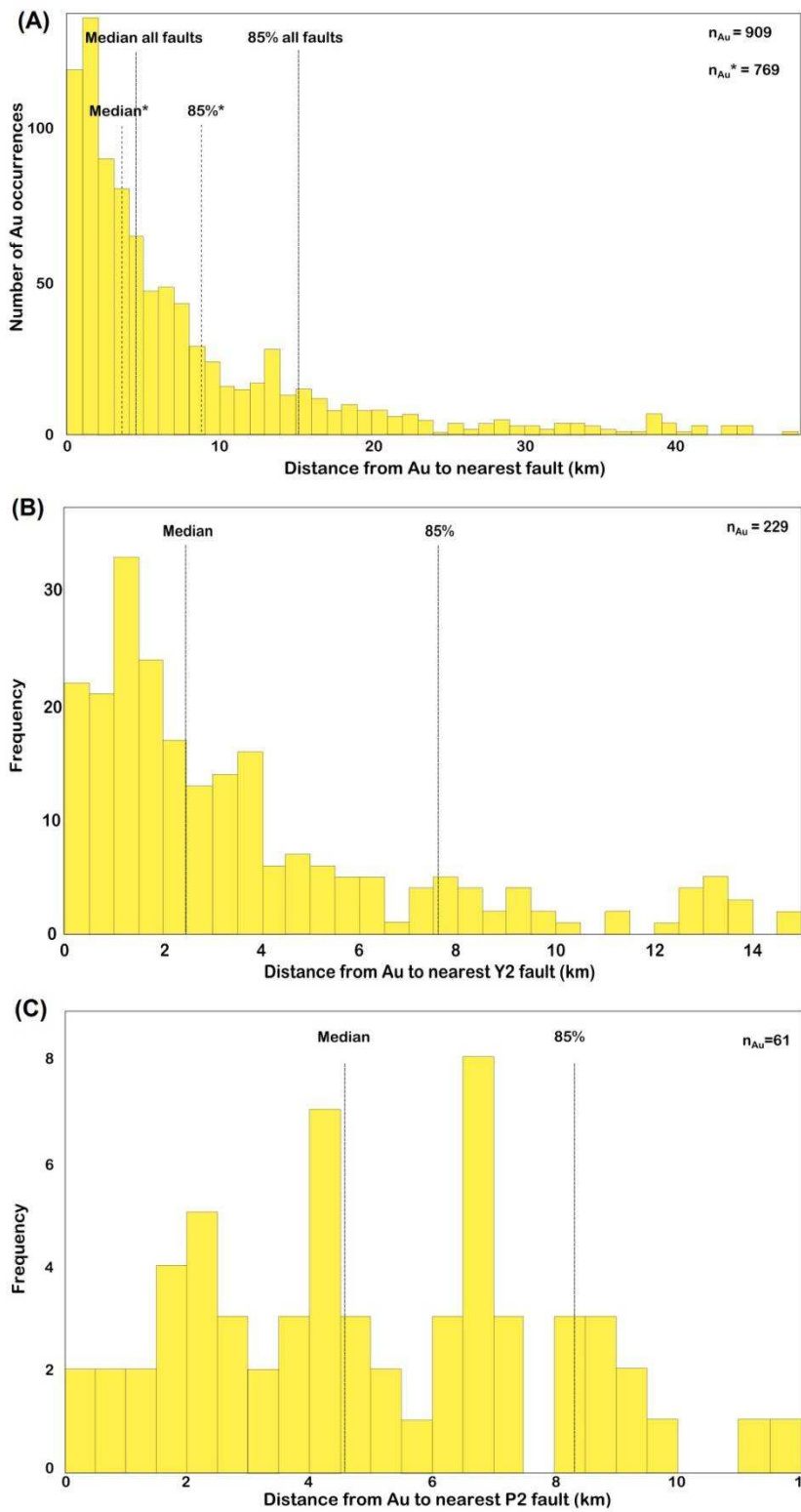
937 Figure 12



938

939

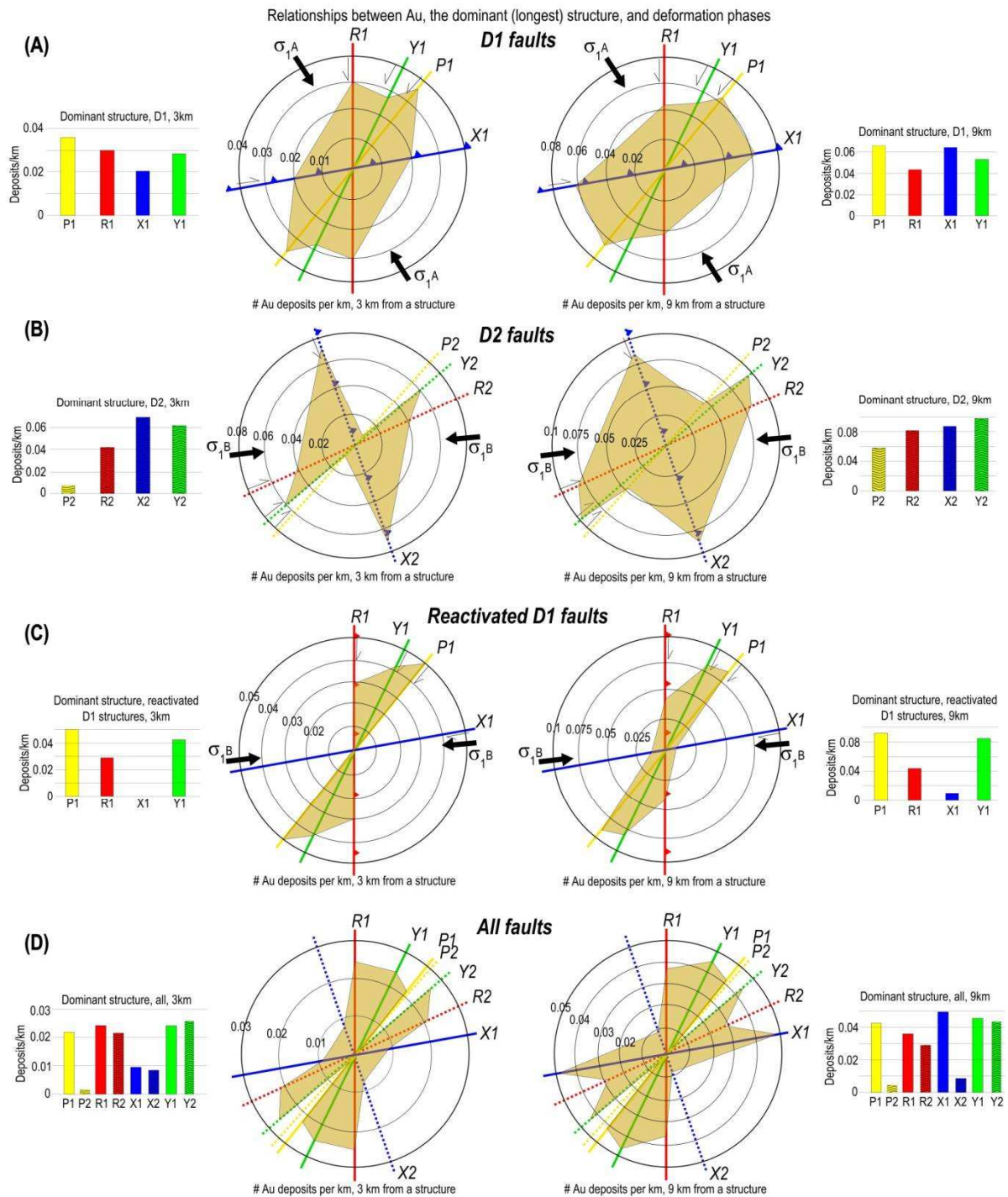
940 Figure 13



941

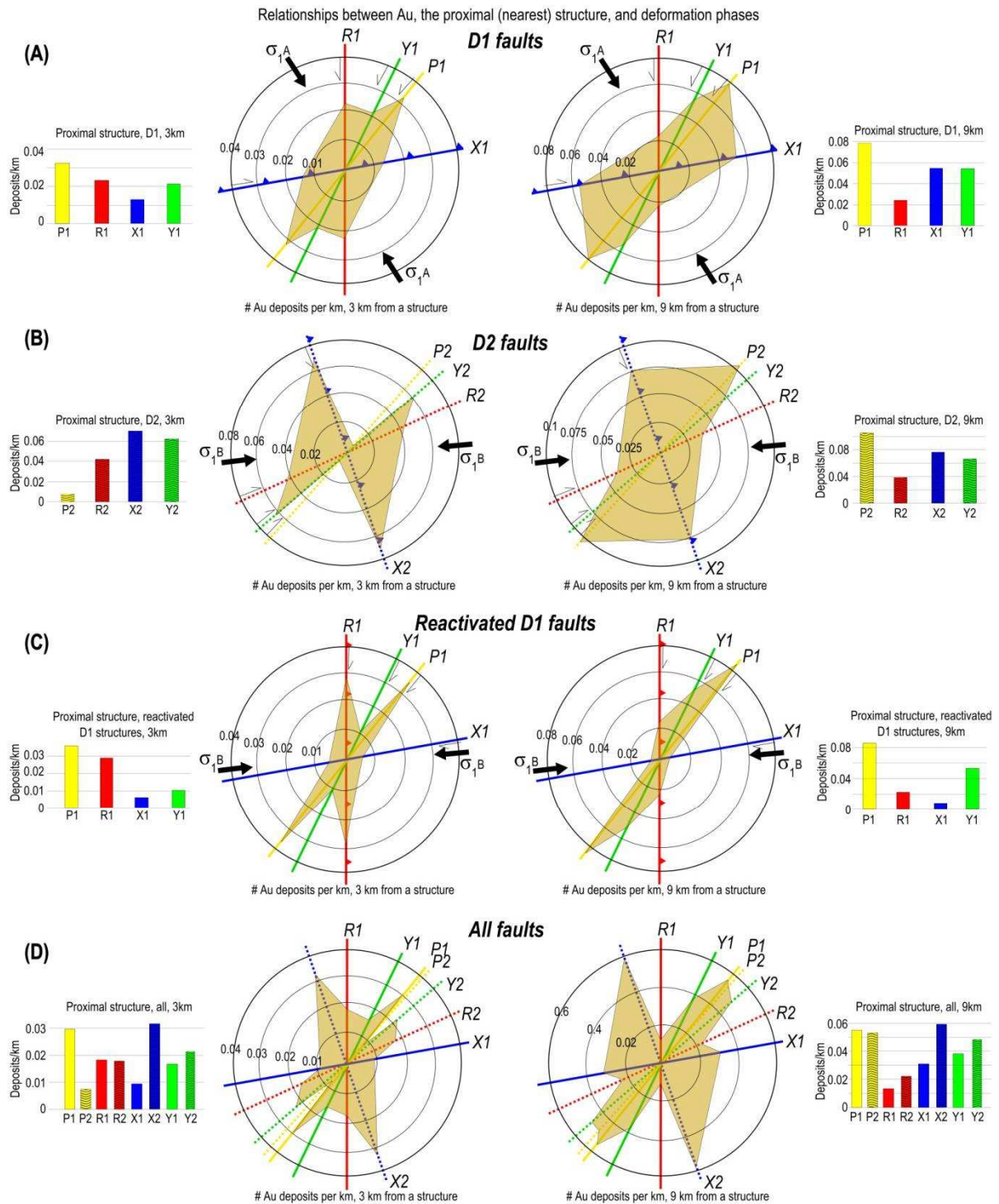
942

943



945

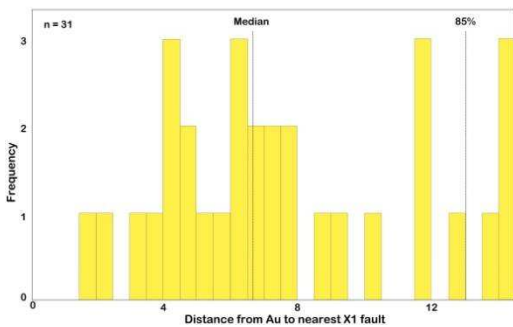
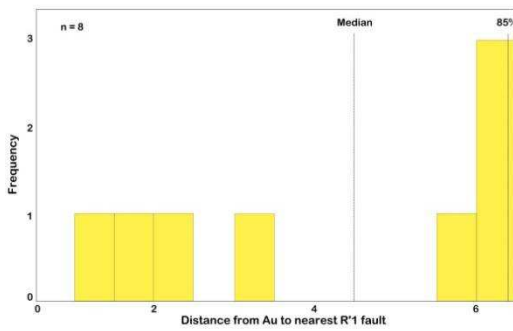
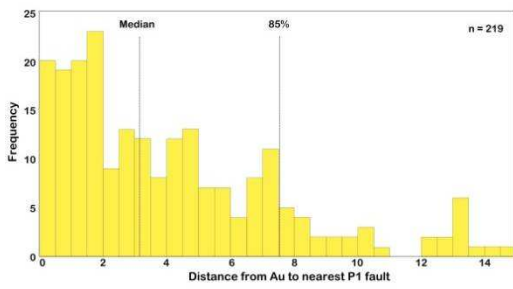
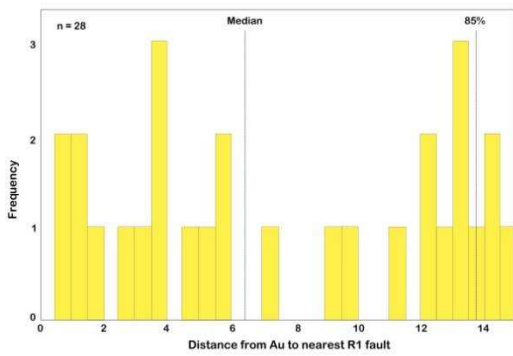
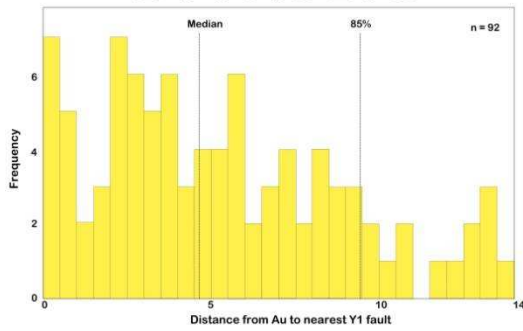
946



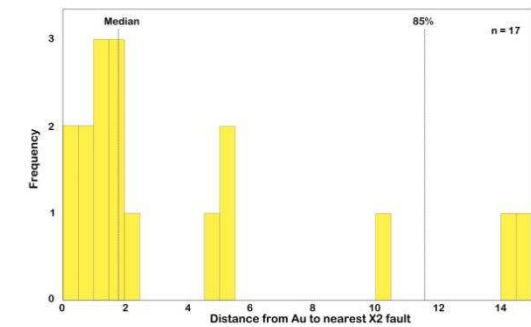
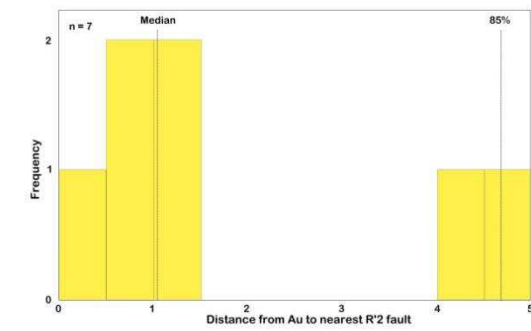
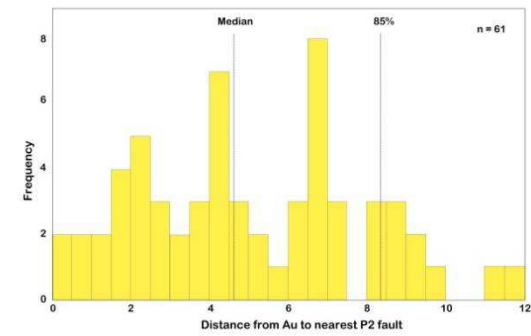
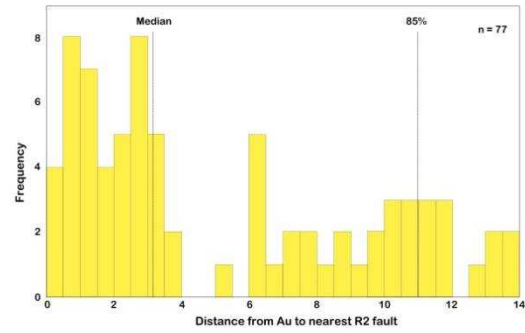
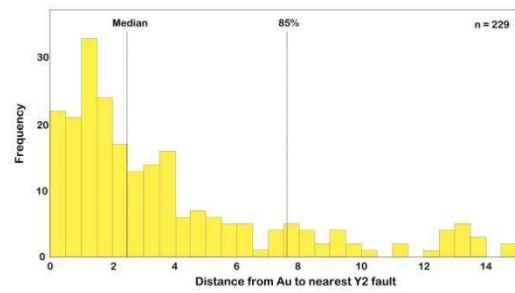
948

949

## D1 FAULTS



## D2 FAULTS



Phase	Age	$\sigma_1$ orientation (present reference frame)	Key events described in literature
D0	c. 2.4-2.2 Ga (early Eburnean phase)	$\sigma_1 = c. \text{WNW-ESE}$	Possible 'keel-and-dome' style basement structure forms Deposition of turbidites and volcanics (the protoliths of the greenstone belts) Possible emplacement of TTG within the greenstone. TTG-greenstone contacts gain a normal sense of movement, N-S fault systems initiate
D1	c. 2.2-2.0 Ga (main Eburnean phase)	$\sigma_1^A = \text{NW-SE}$	Initial thrusting of the Palaeoproterozoic rock on top of the Archean basement and thickening of crust caused by compressional tectonics (until c. 2.1 Ga) Early c. 2.1 Ga leucogranite plutonism from partial melting of TTG and greenstone; compression causes elongation of leucogranites; post-solidification strike-slip shearing dominates (after c. 2.1 Ga) along leucogranite-greenstone contacts Asymmetric folding and syn-metamorphic shear zones N-S/NNE-SSW striking sinistral faults and dominantly SE-dipping thrusts Synchronous with deposition of Tarkwaian conglomerate in the east
D2	2.0-1.8 Ga (post-Eburnean)	$\sigma_1^B = c. \text{E-W}$ (disputed)	NE-SW striking dextral and reverse/thrust faults 330°-trending faults and small drag folds possible

Table 1: Phases of deformation forming the gold-bearing structures in Côte d'Ivoire used in this paper. D0 and D1 are overlapping; also note that, based on published literature, the strike-slip movements of the D1 faults are interpreted to have mainly occurred late during the D1 (mainly post-solidification of the Eburnean leucogranites). The orientation of the maximum principal stress ( $\sigma_1$ ) as indicated in published works for each phase is also indicated. See text for relevant references.

952

953

954

955

956

957

Dataset	Source	Description	Usage
Aeromagnetic – Total magnetic intensity (TMI)	<ul style="list-style-type: none"> <li>• Kenting Exploration Services Ltd.</li> <li>• Aerial survey flown 1974-1976</li> <li>• Fixed-wing aircraft equipped with total field magnetometer and gamma-ray spectrometer.</li> <li>• N-S flight lines at 150m altitude above terrain with 500m line spacing.</li> </ul>	<ul style="list-style-type: none"> <li>• Coverage of most of Côte d'Ivoire in JPEG format</li> <li>• Linear artefacts of the flight lines orientated N-S throughout the dataset.</li> <li>• N-S trending anomalies are of a low magnitude due to low magnetic inclination.</li> <li>• Anisotropy within TMI and VD will have shifted apparent location of structures.</li> </ul>	<ul style="list-style-type: none"> <li>• Corrected for intensity variations of the International Geomagnetic Reference Field (IGRF).</li> <li>• Provide detail and determine structural connectivity.</li> </ul>
Aeromagnetic – Analytical signal (AS)			<ul style="list-style-type: none"> <li>• Corrects for low inclination</li> <li>• Peaks identify correct location of linear structures and boundaries.</li> </ul>
Aeromagnetic – Vertical derivative (VD)			<ul style="list-style-type: none"> <li>• Emphasises maxima and minima.</li> <li>• Provide detail and determine structural connectivity.</li> </ul>
Regional-scale geological maps	<ul style="list-style-type: none"> <li>• Bagarre and Tagini (1965).</li> </ul>	<ul style="list-style-type: none"> <li>• Regional scale 1:1 000 000 geological map.</li> <li>• Fairly generalised.</li> <li>• Dense rainforest coverage causes uncertainty (Mundt, 2016).</li> <li>• Likely to be in need of revision.</li> </ul>	<ul style="list-style-type: none"> <li>• Gain an initial understanding of the lithological and structural trends.</li> </ul>
Local-scale geological maps, Au location maps	<ul style="list-style-type: none"> <li>• A collection of 39 geological maps published by the Direction des Mines et de la Géologie du Gouvernement de la Côte d'Ivoire between 1963 and 1998 (Delor and Yao, 1998)</li> <li>• Au locations collated by ToroGold</li> </ul>	<ul style="list-style-type: none"> <li>• Scales vary between 1:200 000 and 1:500 000.</li> <li>• Map symbology is inconsistent.</li> <li>• Au locations rarely include size, grade, or style of mineralisation.</li> <li>• Some print is unclear.</li> <li>• French geological information – possible translation errors.</li> <li>• Dense rainforest coverage causes uncertainty (Mundt, 2016).</li> <li>• Likely to be in need of revision.</li> <li>• Do not cover whole of Côte d'Ivoire (Fig. 5).</li> </ul>	<ul style="list-style-type: none"> <li>• Identify where AS maxima indicate changes in lithology</li> <li>• Confirm uncertainties in fault kinematics where possible.</li> </ul>

959 Table 2: Data available for the study including descriptions of content, quality, main  
960 uncertainties, and usage in this study.

Structure	Mean strike	Mean length km	Circular variance (CV)	Total count	Median distance to Au occurrence (km) <sup>x</sup>	Active during D2	Reactivation %	Angle between strike and $\sigma_1^A$	Angle between strike and $\sigma_1^B$
Y1	25.5	36.4	0.01	59	4.6	29	49	50.5	59.5
R1	20.5	37.3	0.567	82	6.4	15	18	45.5	64.5
P1	37.5	27.3	0.013	150	3.1	129	86	62.5	47.5
R'1	127.1	14.4	0.035	16	4.5	10	63	27.9	42.1
X1*	79.9	16.6	0.011	121	6.7	21	17	75.1	5.1
Y2	48.5	20	0.006	138	2.5	138	N/A	N/A	36.5
R2	64.5	13.5	0.007	120	3.2	120	N/A	N/A	20.5
P2	41.5	20.5	0.005	33	4.6	33	N/A	N/A	43.5
R'2	111.2	11.0	0.013	10	1.0	10	N/A	N/A	26.2
X2*	160.3	20.5	0.013	23	1.8	23	N/A	N/A	75.3
total				752					
Aver. all		21.75	0.068						
Aver. D1		26.4	0.127						
Aver. D2		17.1	0.009						
Median all		20.25	0.012		3.8				
Median D1		27.3	0.013		4.6				
Median D2		20	0.007		2.5				

962 Table 3. Basic statistics for all interpreted faults. Angles that are approximately within the

963 "reactivation window" for strike-slip faults are highlighted. \*Thrust/reverse faults; x

964 Occurrences within 15 km of a fault only (see text).

965